

Fig. 11.1 (a) The (approximate) observed net average incoming solar radiation and outgoing infrared radiation at the top of the atmosphere, as a function of latitude (plotted on a sine scale). (b) The temperatures associated with these fluxes, calculated using $T = (R/\sigma)^{1/4}$, where R is the solar flux for the radiative equilibrium temperature and R is the infrared flux for the effective emitting temperature. Thus, the solid line is an approximate radiative equilibrium temperature

From Vallis (2006)

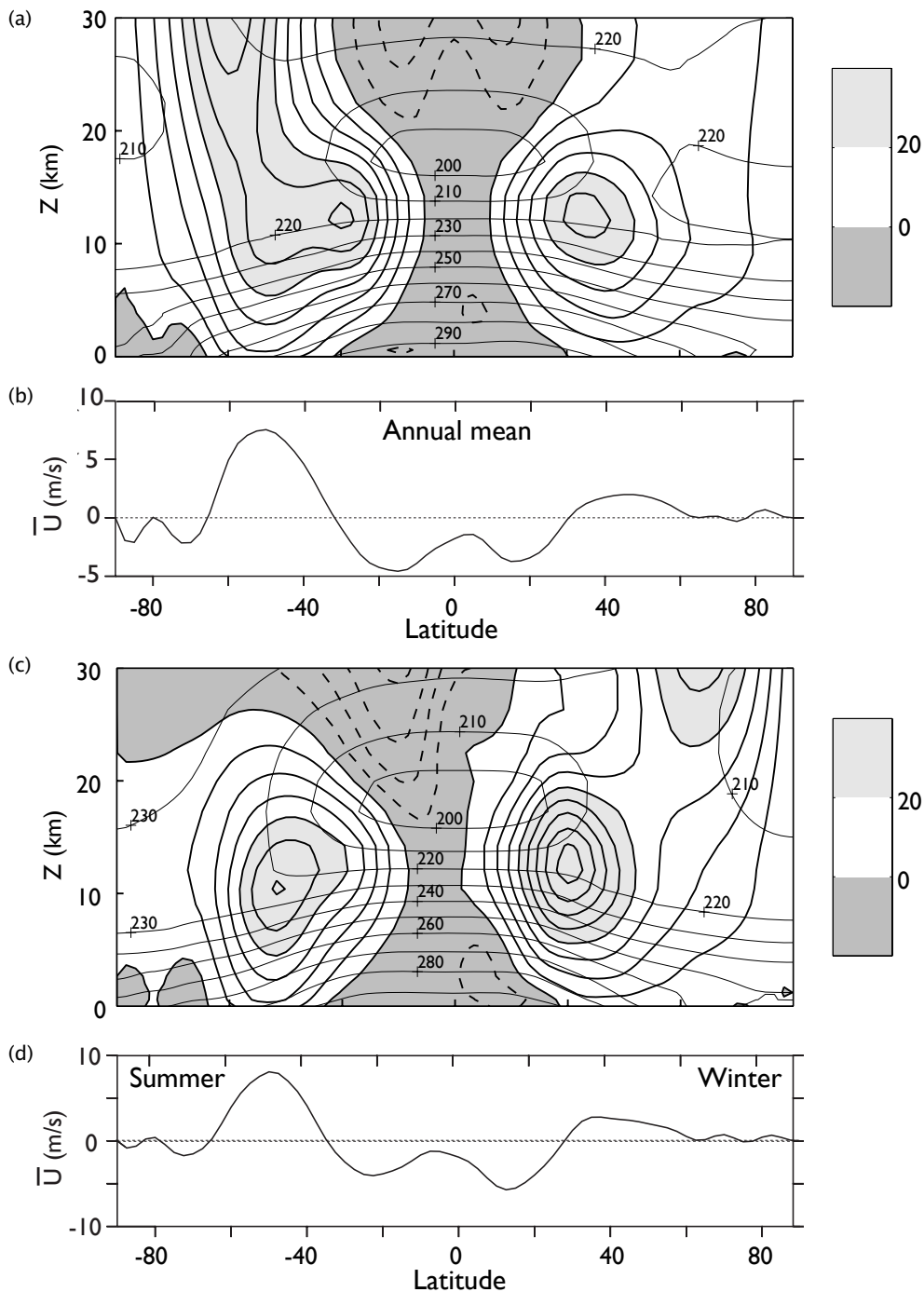


Fig. 11.2 (a) Annual mean, zonally averaged zonal wind (heavy contours and shading) and the zonally averaged temperature (lighter contours). (b) Annual mean, zonally averaged zonal winds at the surface. (c) and (d) Same as (a) and (b), except for northern hemisphere winter (DJF). The wind contours are at intervals of 5 m s^{-1} with shading for eastward winds above 20 m s^{-1} and for all westward winds, and the temperature contours are labelled. The ordinate of (a) and (c) is $Z = -H \log(p/p_R)$, where p_R is a constant, with scale height $H = 7.5 \text{ km}$.

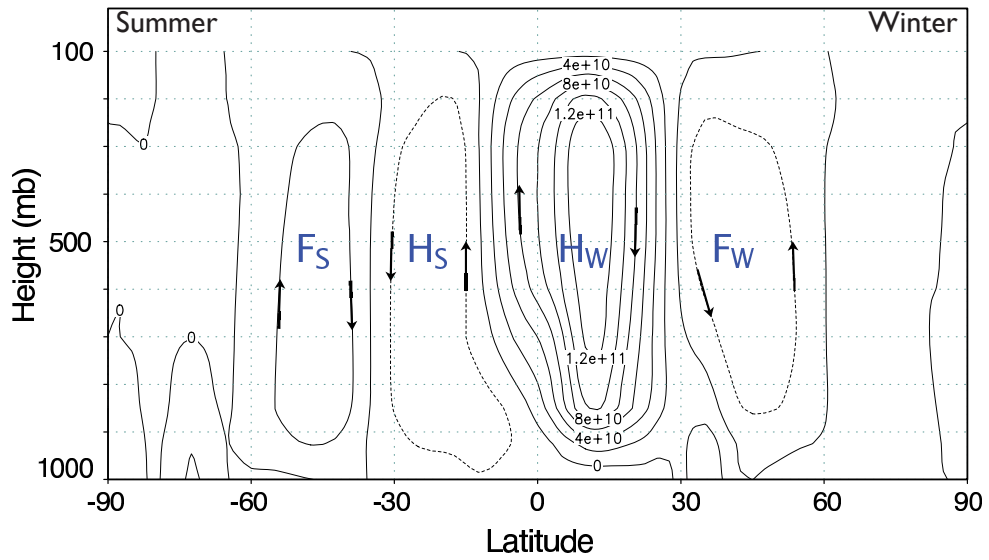


Fig. 11.3 The observed, zonally averaged, meridional overturning circulation of the atmosphere, in units of kg s^{-1} , averaged over December–January–February (DJF). In each hemisphere note the presence of a direct *Hadley Cell* (H_W and H_S in winter and summer) with rising motion near the equator, descending motion in the subtropics, and an indirect *Ferrel Cell* (F_W and F_S) at mid-latitudes. There are also hints of a weak direct cell at high latitudes. The winter Hadley Cell is far stronger than the summer one.

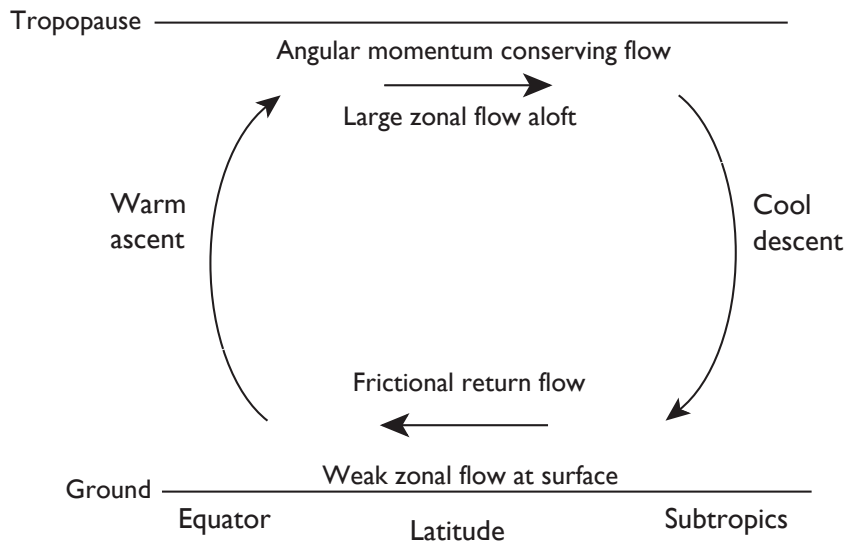


Fig. 11.4 A simple model of the Hadley Cell. Rising air near the equator moves polewards near the tropopause, descending in the subtropics and returning near the surface. The polewards moving air conserves its axial angular momentum, leading to a zonal flow that increases away from the equator. By the thermal wind relation the temperature of the air falls as it moves poleward, and to satisfy the thermodynamic budget it sinks in the subtropics. The return flow at the surface is frictionally retarded and small.

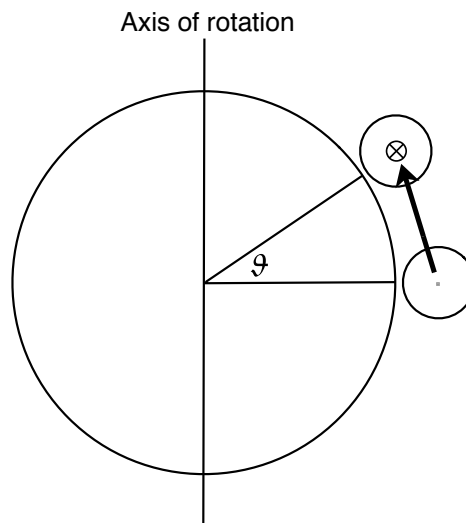


Fig. 11.5 If a ring of air at the equator moves polewards it moves closer to the axis of rotation. If the parcels in the ring conserve their angular momentum their zonal velocity must increase; thus, if $m = (\bar{u} + \Omega a \cos \vartheta)a \cos \vartheta$ is preserved and $\bar{u} = 0$ at $\vartheta = 0$ we recover (11.7).

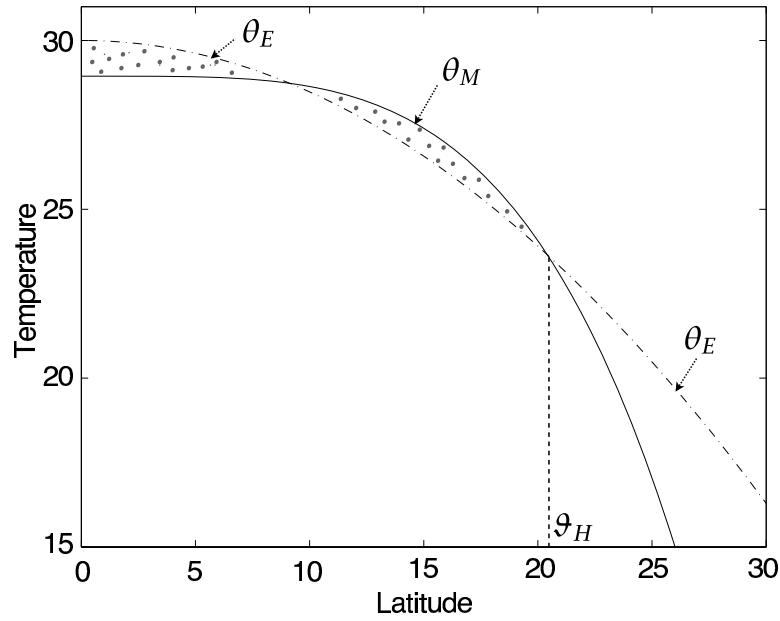


Fig. 11.6 The radiative equilibrium temperature (θ_E , dashed line) and the angular-momentum-conserving solution (θ_M , solid line) as a function of latitude. The two dotted regions have equal areas. The parameters are: $\theta_{E0} = 303$ K, $\Delta\theta = 50$ K, $\theta_0 = 300$ K, $\Omega = 7.272 \times 10^{-5} \text{ s}^{-1}$, $g = 9.81 \text{ m s}^{-2}$, $H = 10$ km. These give $R = 0.076$ and $Y_H/a = 0.356$, corresponding to $\vartheta_H = 20.4^\circ$.

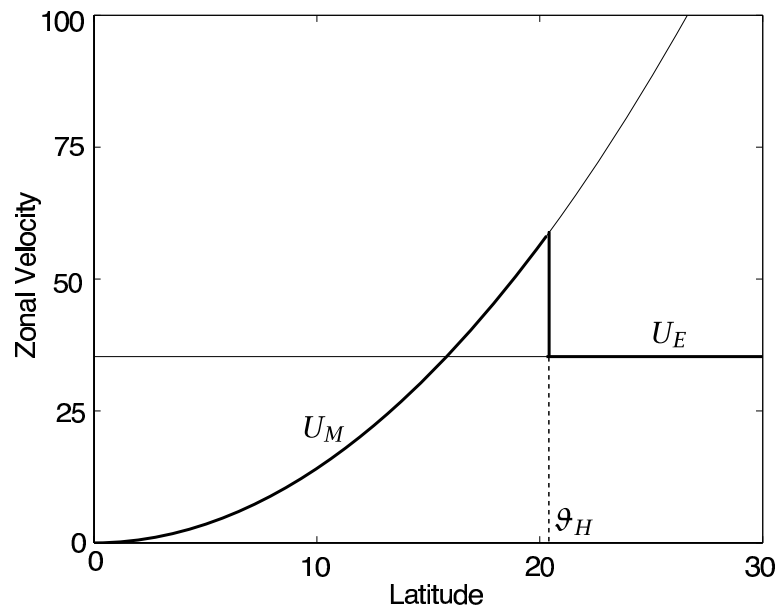


Fig. 11.7 The zonal wind corresponding to the radiative equilibrium temperature (U_E) and the angular-momentum-conserving solution (U_M) as a function of latitude, given (11.25) and (11.26) respectively. The parameters are the same as those of Fig. 11.6, and the radiative equilibrium wind, U_E is a constant, ΩaR . The actual zonal wind (in the model) follows the thick solid line.

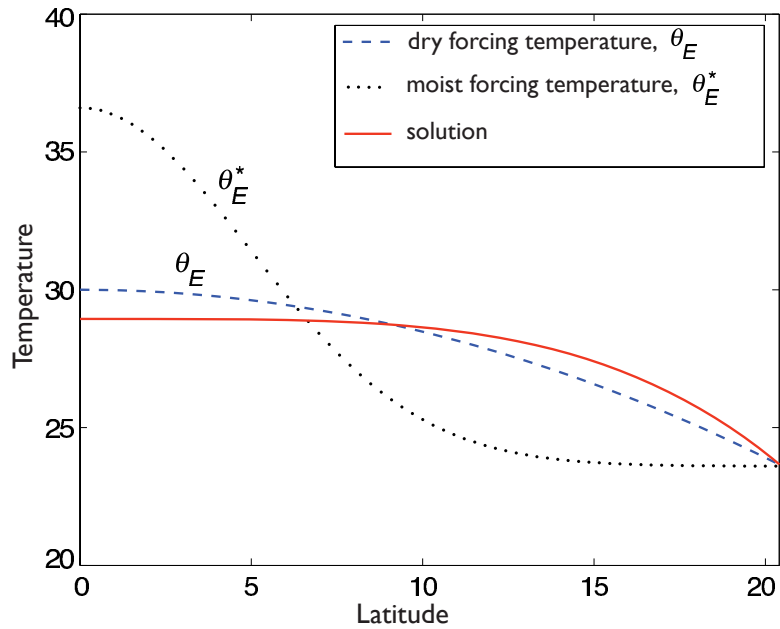


Fig. 11.8 Schema of the effects of moisture on a model of the Hadley Cell. The temperature of the solution (solid line) is the same as that of a dry model, because this is determined from the angular-momentum-conserving wind. The heating distribution (as parametrized by a forcing temperature) is peaked near the equator in the moist case, leading to a more vigorous overturning circulation.

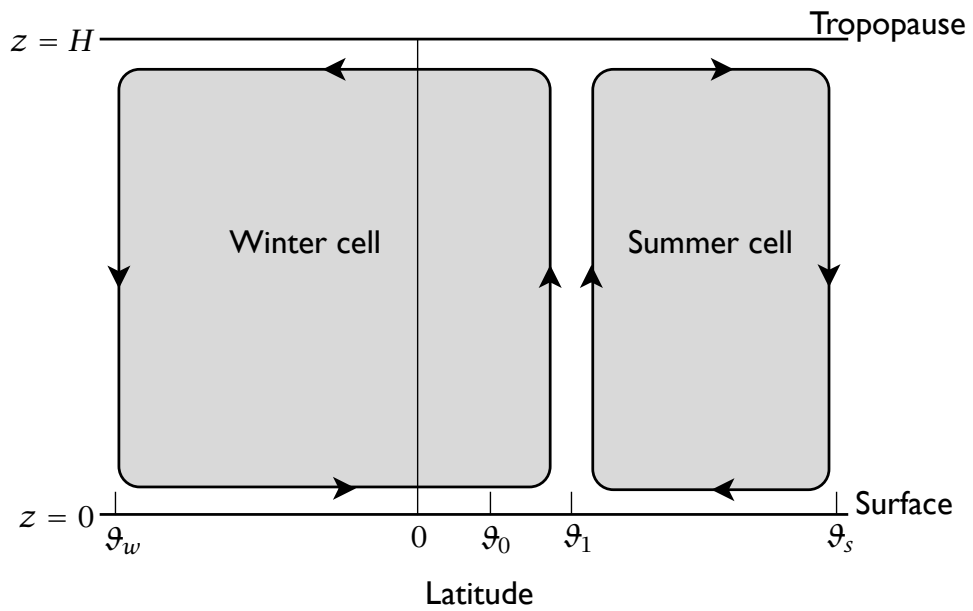


Fig. 11.9 Schematic of a Hadley circulation model when the heating is centred off the equator, at a latitude ϑ_0 . The lower level convergence occurs at a latitude ϑ_1 that is not in general equal to ϑ_0 . The resulting winter Hadley Cell is stronger and wider than the summer cell.

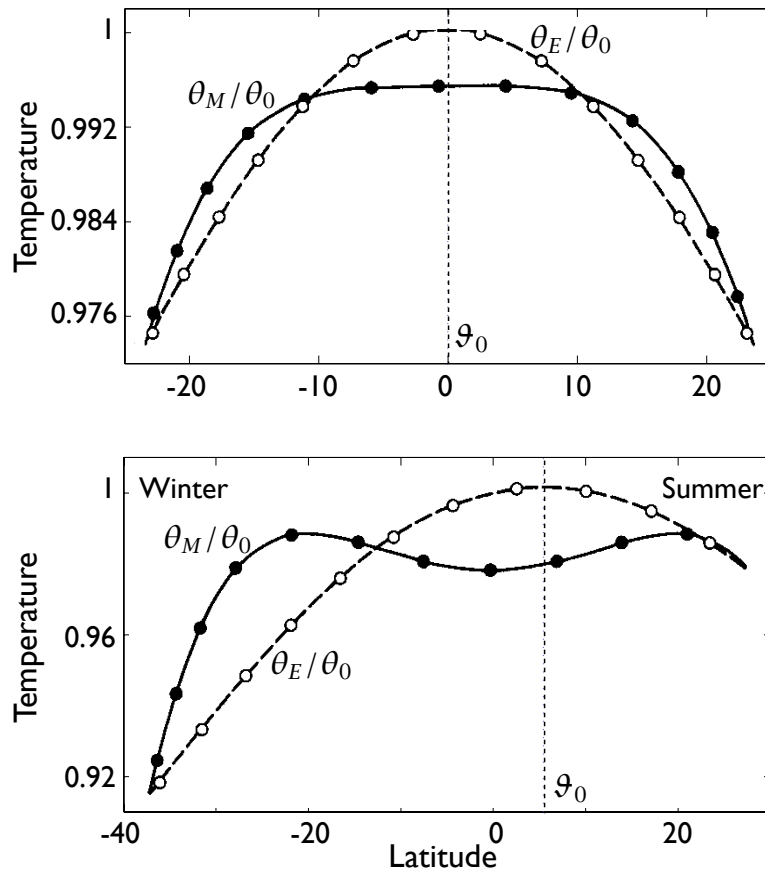


Fig. 11.10 Solutions of the Hadley Cell model with heating centred at the equator ($\vartheta_0 = 0^\circ$, top) and off the equator ($\vartheta_0 = +6^\circ$ N, bottom), with $\Delta_H = 1/6$. The dashed line is the radiative equilibrium temperature and the solid line is the angular-momentum-conserving solution. In the lower panel, $\vartheta_1 \approx +18^\circ$, and the circulation is dominated by the cell extending from $+18^\circ$ to -36° .¹

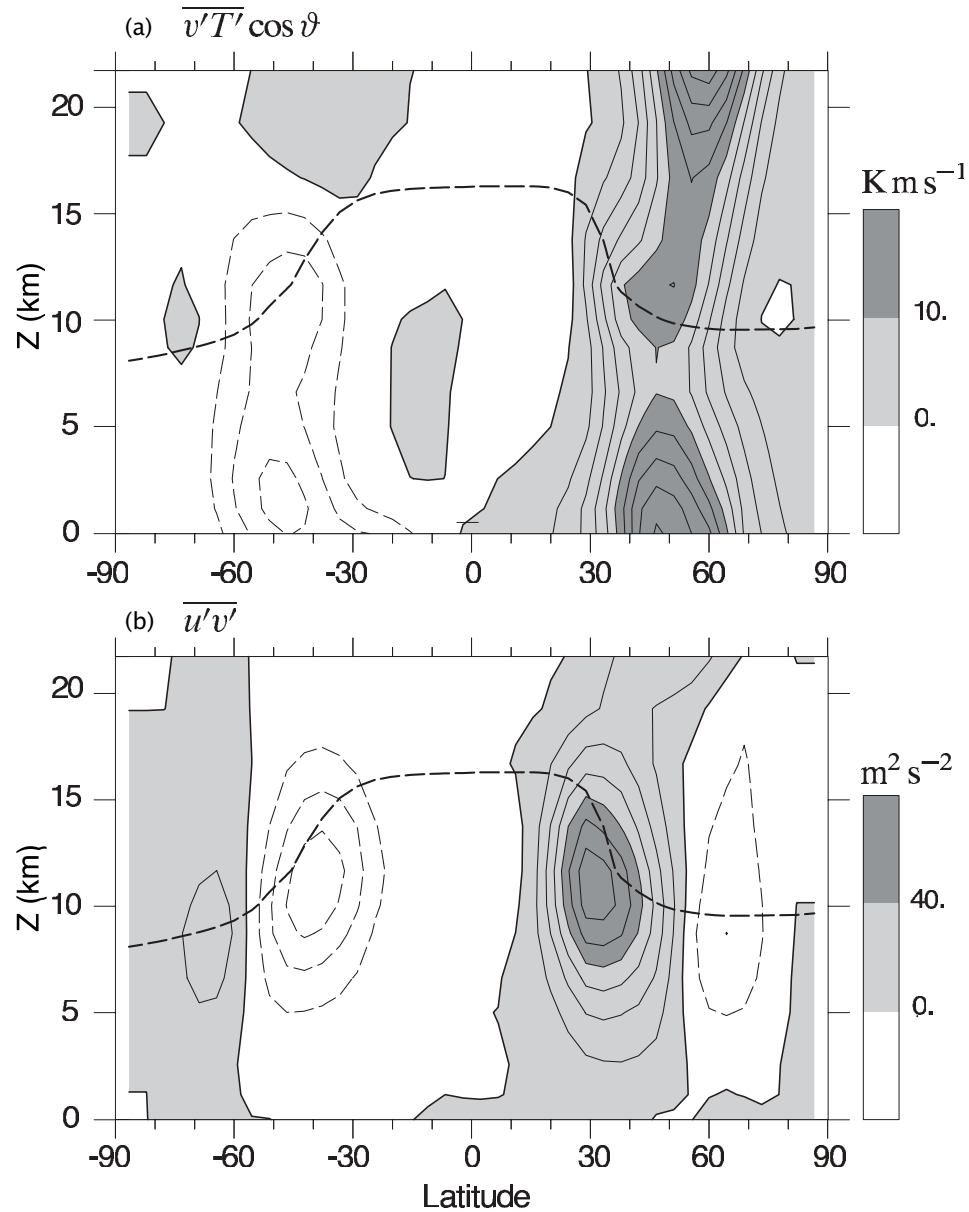


Fig. 11.11 (a) The average meridional eddy heat flux and (b) and the eddy momentum flux in the northern hemisphere winter (DJF). The ordinate is log-pressure, with scale height $H = 7.5$ km. Positive (northward) fluxes are shaded in both cases, and the dashed line marks the thermal tropopause. The eddy heat flux (contour interval 2 K m s^{-1}) is largely polewards, and down the temperature gradient, in both hemispheres. The eddy momentum flux (contour interval $10 \text{ m}^2 \text{ s}^{-2}$) converges in mid-latitudes in the region of the mean jet, and must be upgradient there.²

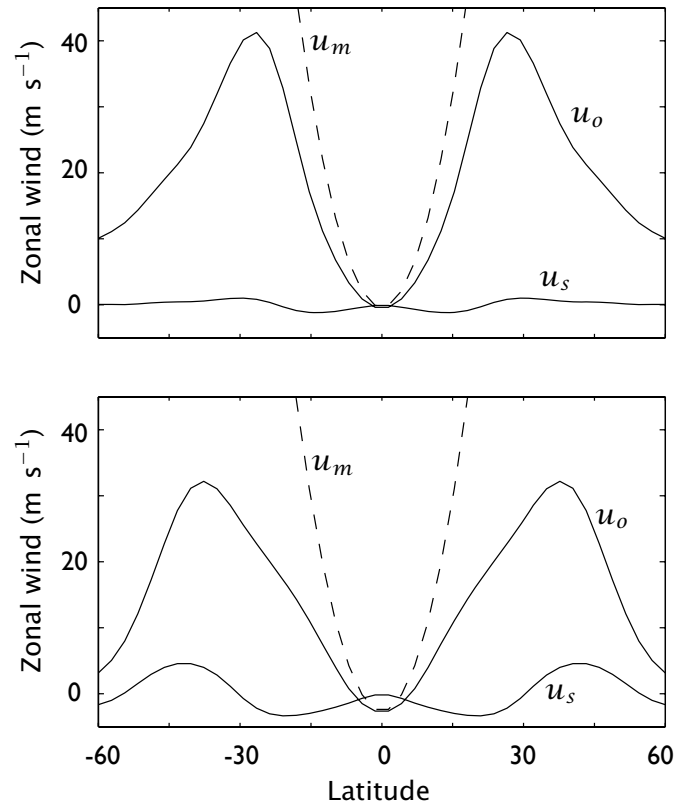


Fig. 11.12 The zonal wind in two numerical simulations. The lower panel is from an idealized dry, three-dimensional atmospheric GCM, and the upper panel is an axisymmetric version of the same model. Plotted are the zonal wind at the level of the Hadley Cell outflow, u_o ; the surface wind, u_s ; and the angular-momentum-conserving value, u_m .³

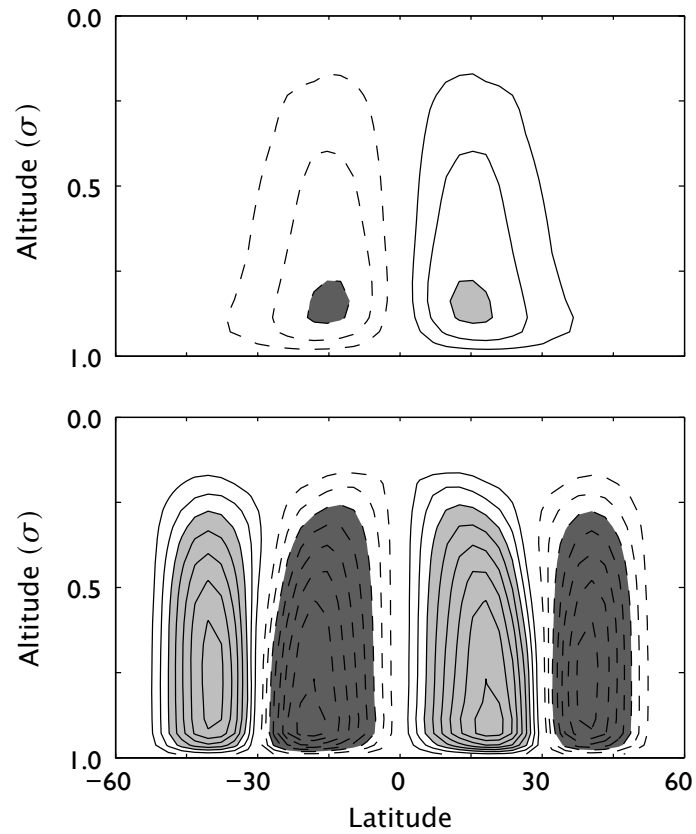


Fig. 11.13 As for Fig. 11.12, but now showing the streamfunction of the overturning circulation. 'Altitude' is $\sigma = p/p_s$, where p_s is surface pressure, and contour interval is 5 Sv (i.e., $5 \times 10^9 \text{ kg s}^{-1}$).

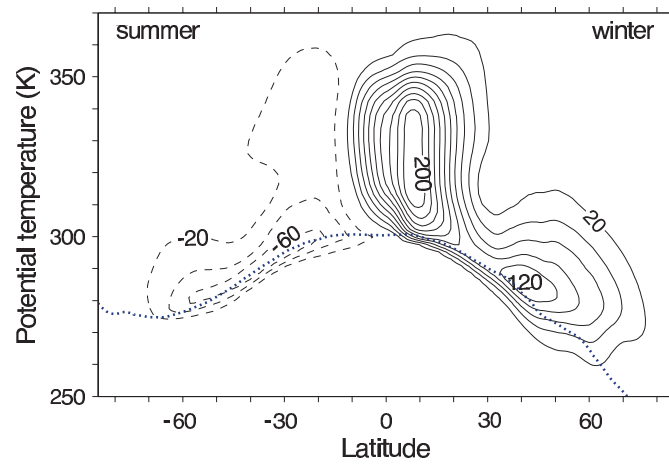


Fig. 11.14 The observed mass transport streamfunction in isentropic coordinates in northern hemisphere winter (DJF). The dotted line is the median surface temperature. The return flow is nearly all in a layer near the surface, much of it at a lower temperature than the median surface temperature. Note the more vigorous circulation in the winter hemisphere.⁴

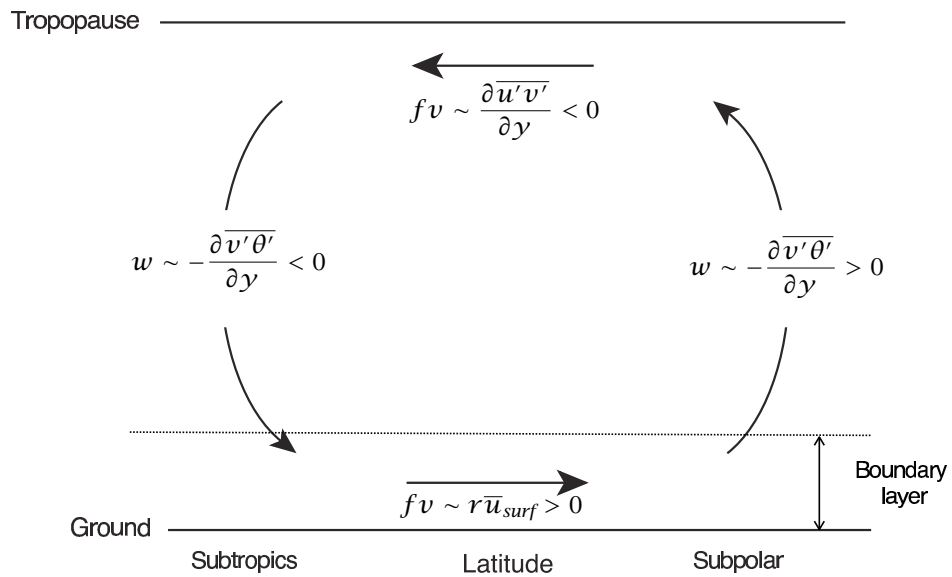


Fig. 11.15 The eddy-driven Ferrel Cell, from an Eulerian point of view. Above the planetary boundary layer the mean flow is largely in balance with the eddy heat and momentum fluxes, as shown. The lower branch of the Ferrel Cell is largely confined to the boundary layer, where it is in a frictional-geostrophic balance.

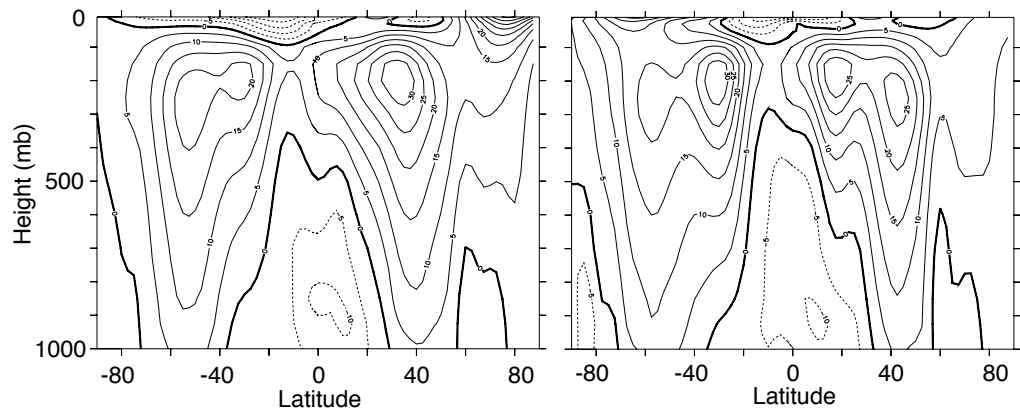


Fig. 12.1 The time averaged zonal wind at 150°W (in the mid-Pacific) in December-January-February (DJF, left), March-April-May (MAM, right). The contour interval is 5 m s⁻¹. Note the double jet in each hemisphere, one in the subtropics and one in mid-latitudes. The subtropical jets are associated with a strong meridional temperature gradient, whereas the mid-latitude jets have a stronger barotropic component and are associated with westerly winds at the surface.

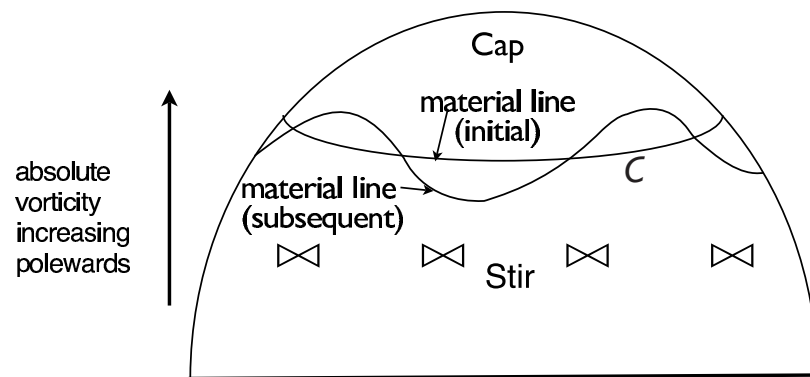


Fig. 12.2 The effects of a mid-latitude disturbance on the circulation around the latitude line C. If initially the absolute vorticity increases monotonically polewards, then the disturbance will bring fluid with lower absolute vorticity into the cap region. Then, using Stokes theorem, the velocity around the latitude line C will become more westward.

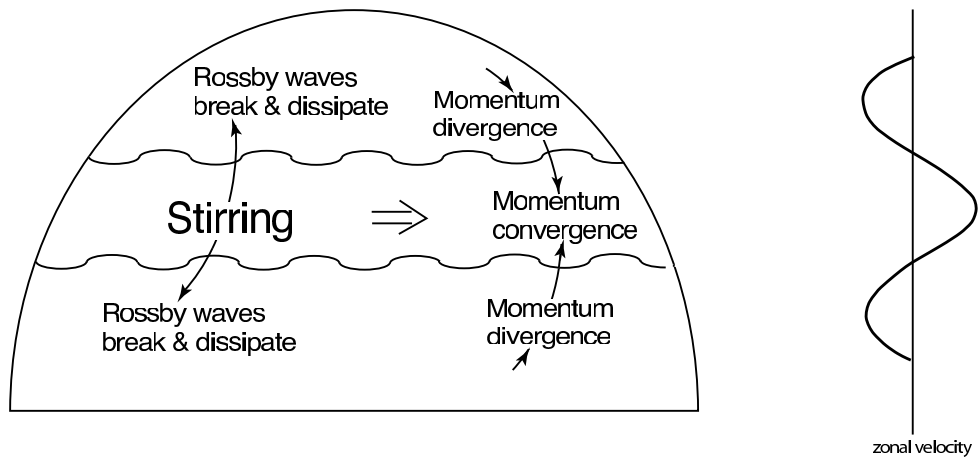


Fig. 12.3 Generation of zonal flow on a β -plane or on a rotating sphere. Stirring in mid-latitudes (by baroclinic eddies) generates Rossby waves that propagate away from the disturbance. Momentum converges in the region of stirring, producing eastward flow there and weaker westward flow on its flanks.

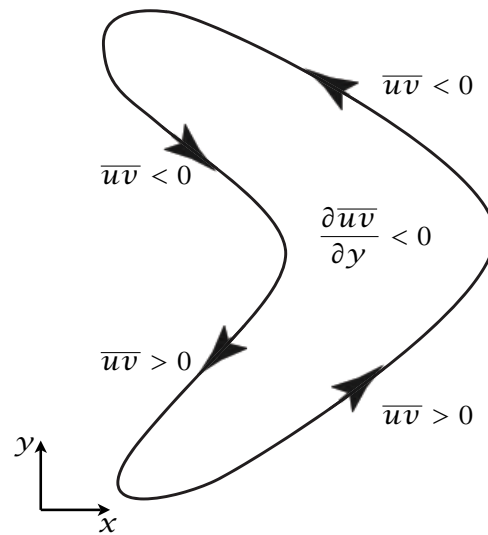


Fig. 12.4 The momentum transport in physical space, caused by the propagation of Rossby waves away from a source in mid-latitudes. The ensuing bow-shaped eddies are responsible for a convergence of momentum, as indicated in the idealization pictured.

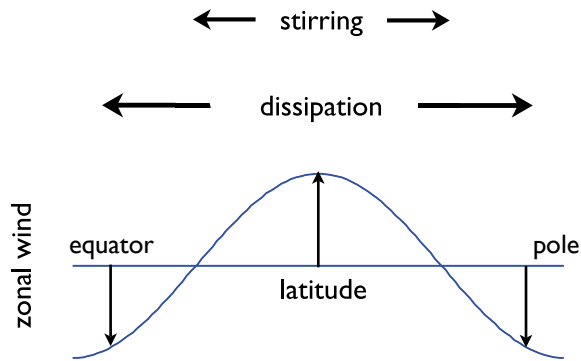


Fig. 12.5 Mean flow generation by a meridionally confined stirring. Because of Rossby wave propagation away from the source region, the distribution of pseudomomentum dissipation is a broader than that of pseudomomentum forcing, and the sum of the two leads to the zonal wind distribution shown, with positive (eastward) values in the region of the stirring. See also Fig. 12.8.

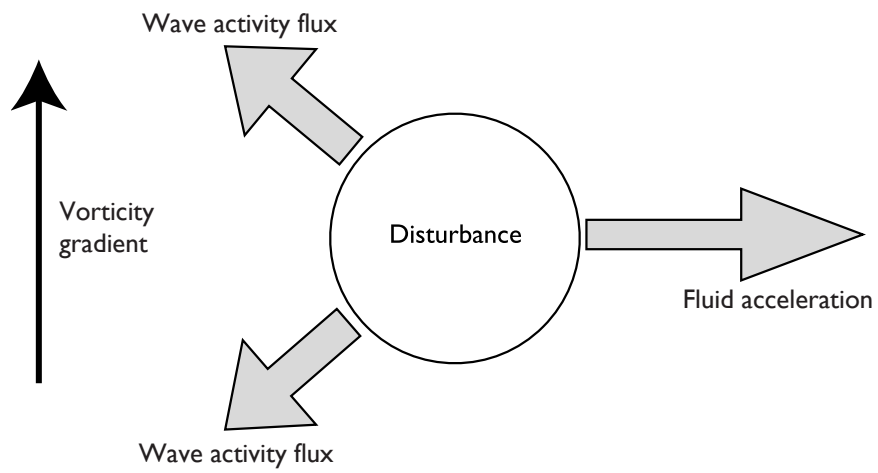


Fig. 12.6 If a region of fluid on the β -plane or on a rotating sphere is stirred, then Rossby waves propagate away from the disturbance, and this is the direction of the wave activity density flux vector. Thus, there is divergence of wave activity in the stirred region, and using (12.35) this produces an eastward acceleration.

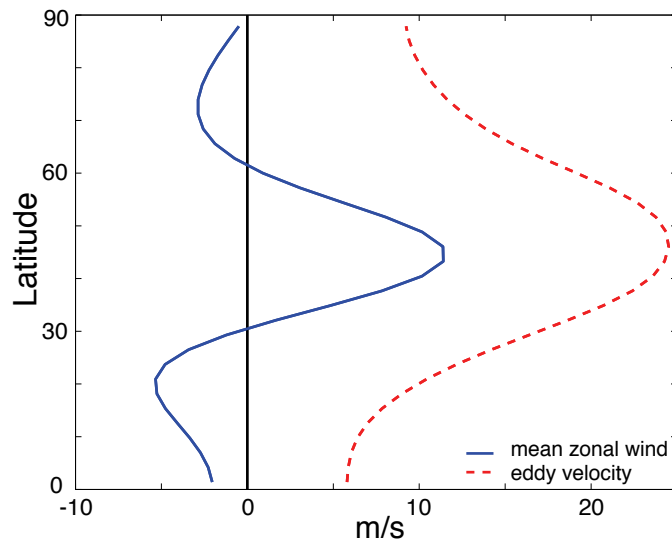


Fig. 12.7 The time and zonally averaged wind (solid line) obtained by an integration of the barotropic vorticity equation (12.37) on the sphere. The fluid is stirred in mid-latitudes by a random wavemaker that is statistically zonally uniform, acting around zonal wavenumber 8, and that supplies no net momentum. Momentum converges in the stirring region leading to an eastward jet with a westward flow to either side, and zero area-weighted spatially integrated velocity. The dashed line shows the r.m.s. (eddy) velocity created by the stirring.

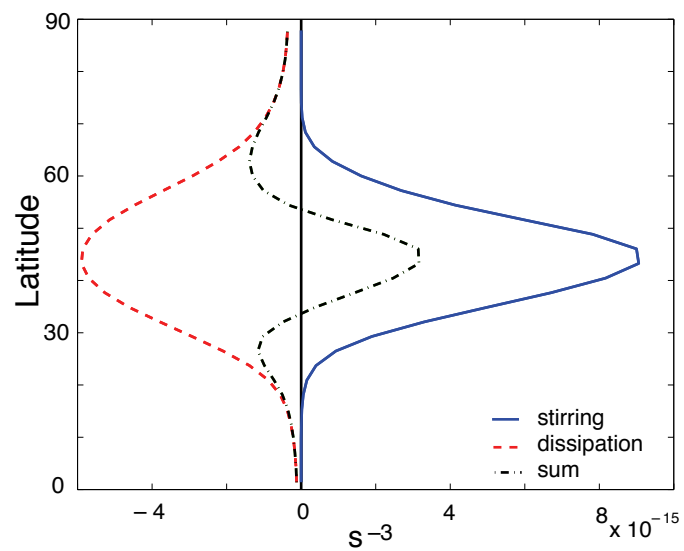


Fig. 12.8 The pseudomomentum stirring (solid line, $\overline{F'_\zeta \zeta'}$), dissipation (dashed line, $\overline{D'_\zeta \zeta'}$) and their sum (dot-dashed), for the same integration as Fig. 12.7. Because Rossby waves propagate away from the stirred region before breaking, the distribution of dissipation is broader than the forcing, resulting in an eastward jet where the stirring is centred, with westward flow on either side.

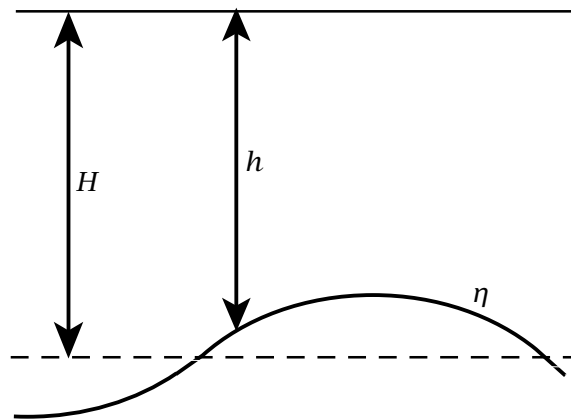


Fig. 12.9 A model atmosphere with an active layer of mean thickness H , local thickness h , and a variable lower surface of height displacement η , lying above a stationary layer with a slightly larger potential density.

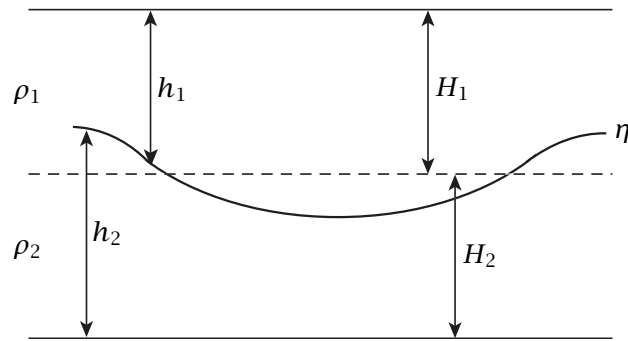


Fig. 12.11 An atmosphere with two homogeneous (or isentropic) layers of mean thickness H_1 and H_2 , local thickness h_1 and h_2 , and interface η , contained between two flat, rigid surfaces.

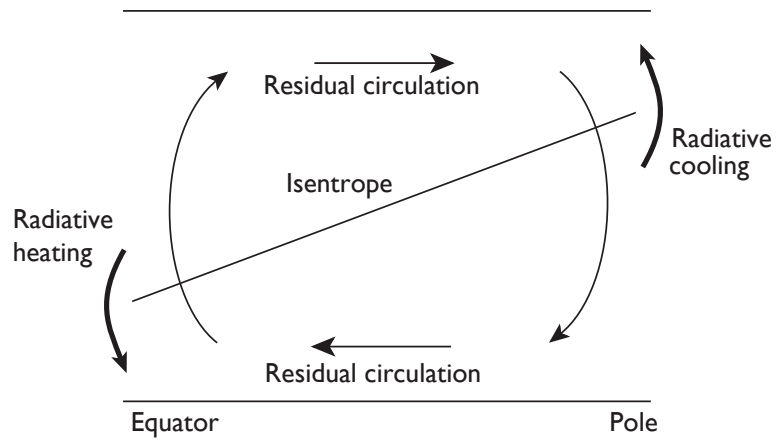


Fig. 12.12 Sketch of the zonally averaged thermodynamics of a two-layer model. Cooling at high latitudes and heating at low ones steepens the interface upward toward the pole (thicker arrows). Associated with this is a net mass flux — the residual flow, or the meridional overturning circulation (lighter arrows). In the tropics this circulation is accounted for by the Hadley Cell, and is nearly all in the mean flow. In mid-latitudes the circulation — the residual flow — is largely due to baroclinic eddies, and the smaller Eulerian mean flow is actually in the opposite sense.

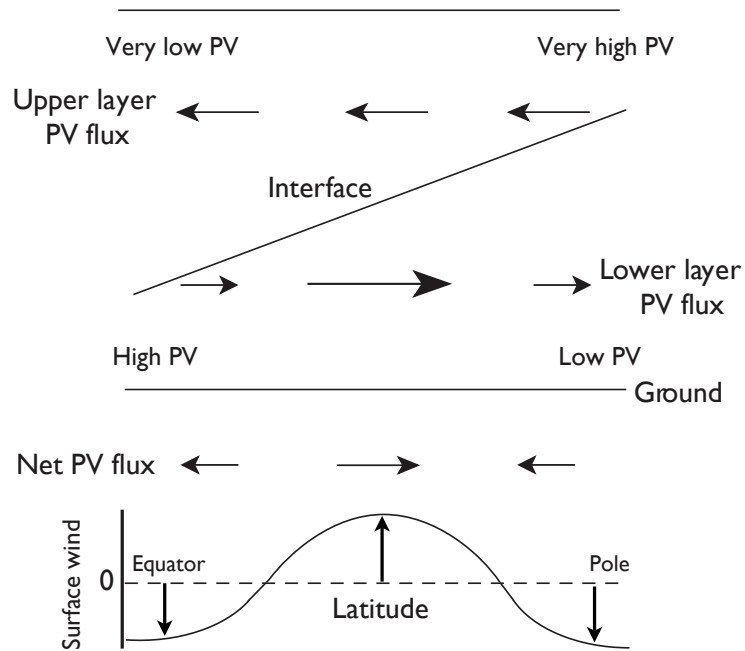


Fig. 12.13 Sketch of the potential vorticity fluxes in a two-layer model. The surface wind is proportional to their vertical integral. The PV fluxes are negative (positive) in the upper (lower) layer, but are more uniformly distributed at upper levels. The lower panel shows the net (vertically integrated) PV fluxes and the associated surface winds.

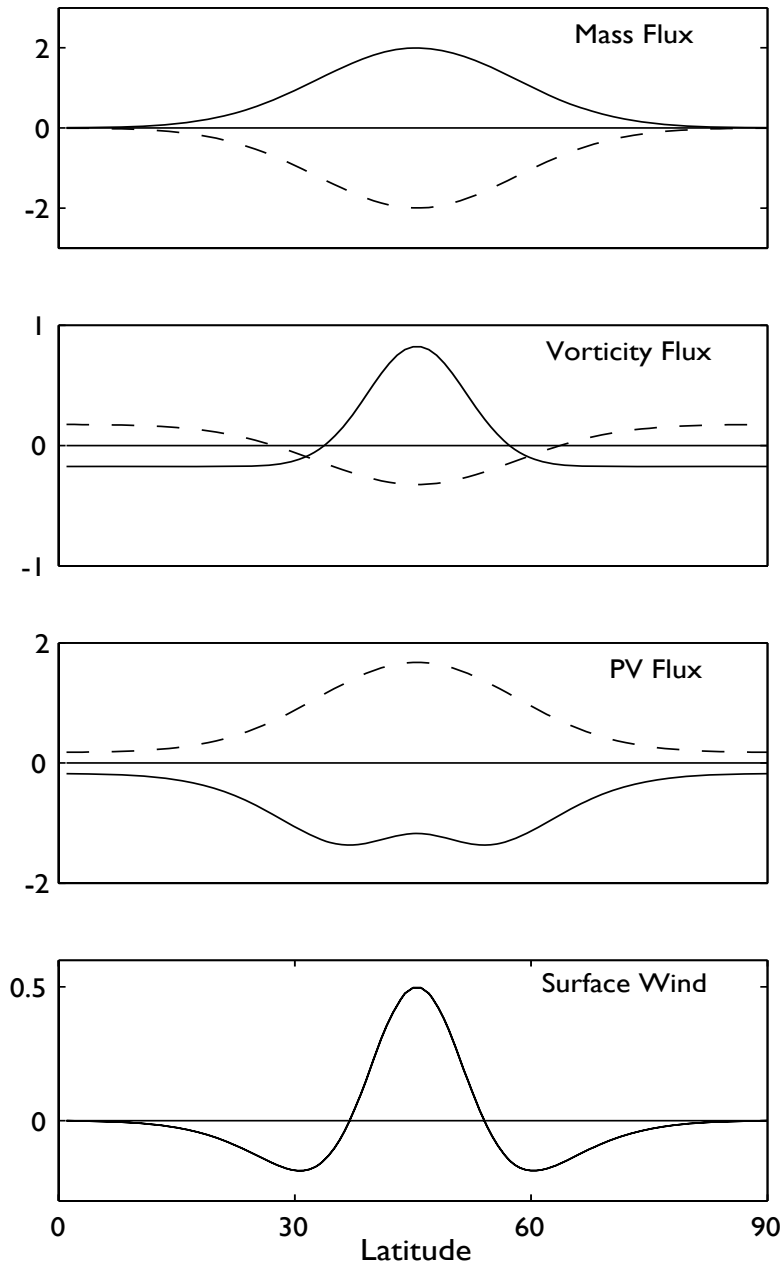


Fig. 12.14 Schema of the eddy fluxes in a two-layer model of an atmosphere with a single mid-latitude baroclinic zone. The upper-layer fluxes are solid lines and the lower-layer fluxes are dashed. The lowest panel shows the sum of the lower- and upper-layer vorticity fluxes (or, equivalently, the sum of the potential vorticity fluxes), which is proportional (when the surface friction is a linear drag) to the surface wind. The fluxes satisfy the various relationships and integral constraints of section 12.2.2 but are otherwise idealized.

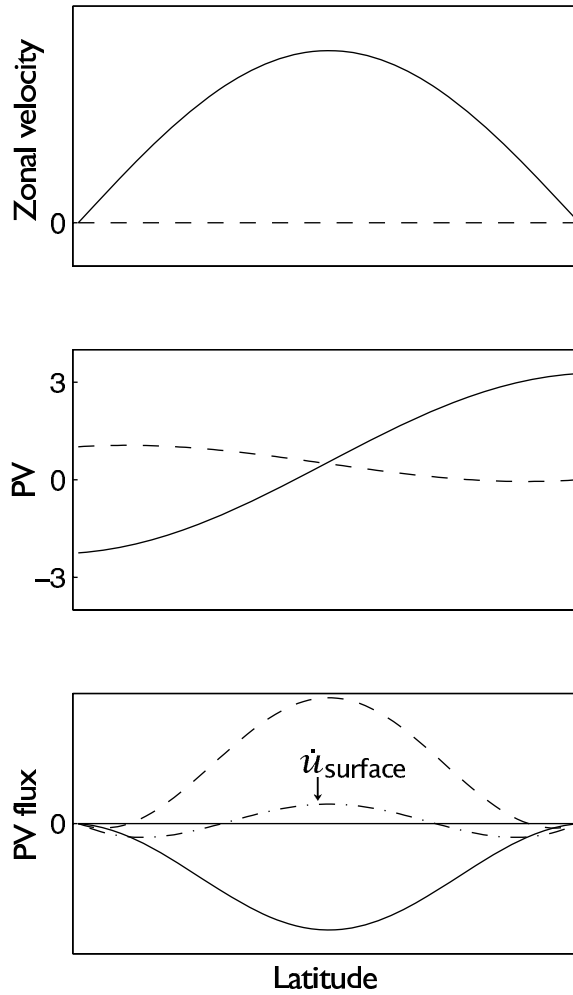


Fig. 12.15 Results from a diffusive closure in a two-layer zonally averaged model. Upper-layer quantities are solid lines and lower-layer quantities are dashed. The initial zonally averaged zonal velocity (top panel) is large in the upper layer and zero in the lower layer. This produces the potential vorticity structure illustrated in the middle panel, in units in which $\beta = 1$. A diffusive closure of the form (12.99) then produces the potential vorticity fluxes illustrated at the bottom, where the sum of the fluxes in the two layers is the dot-dashed line, and this is proportional to the tendency of the zonal wind. The residual circulation is proportional to the negative of the PV flux, and so is poleward in the upper layer and equatorward in the lower layer. The vertical structure of the diffusivity is chosen such that (12.82) is satisfied.

From Vallis (2006)

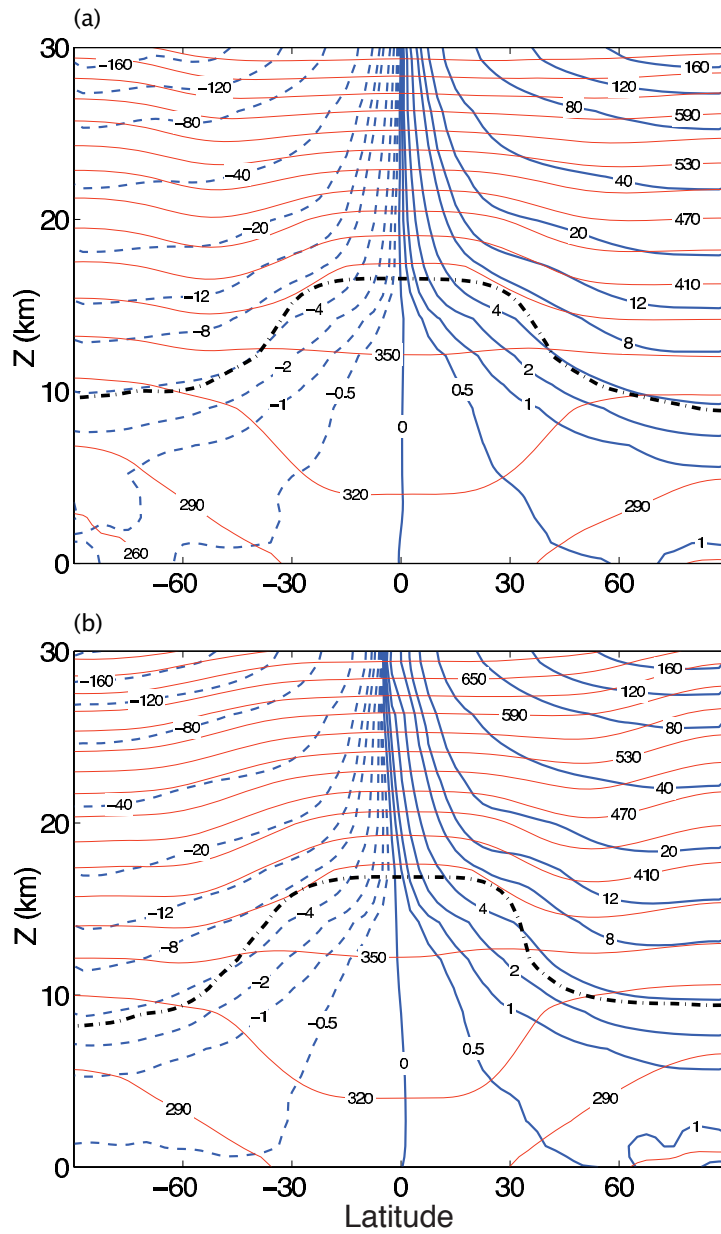


Fig. 12.16 The observed zonally averaged Ertel potential vorticity distribution (thicker, solid and dashed lines, peaking up at the equator) and the potential temperature (lighter lines) for (a) annual mean, (b) December-January-February. Also shown is the position of the WMO thermal tropopause (dot-dashed line). The potential vorticity is in 'PV units': $1 \text{ PVU} \equiv 1.0 \times 10^{-6} \text{ m}^2 \text{ K s}^{-1} \text{ kg}^{-1}$. Note the uneven contour interval for potential vorticity. The vertical coordinate is log pressure, with $Z = -7.5 \log(p/p_R) \text{ km}$, where $p_R = 10^5 \text{ Pa}$.

From Vallis (2006)

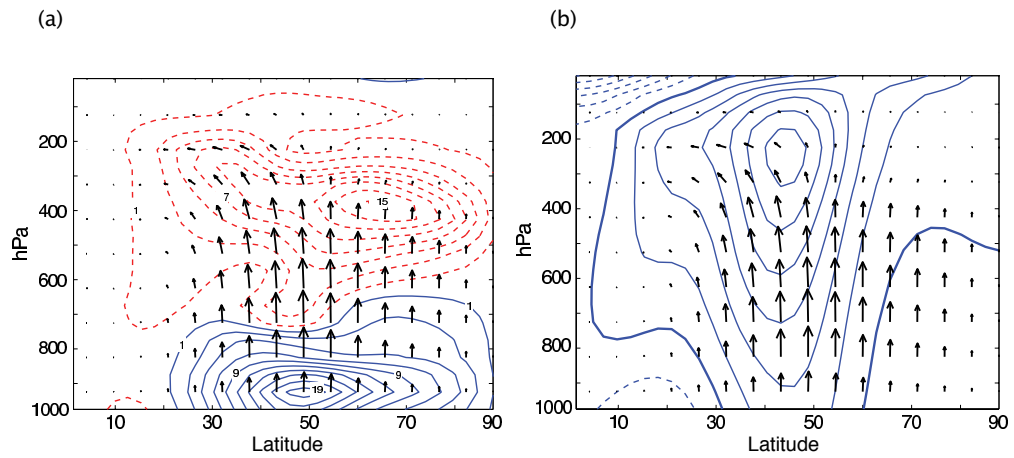


Fig. 12.17 The Eliassen-Palm flux in an idealized primitive equation of the atmosphere. (a) The EP flux (arrows) and its divergence (contours, with intervals of $2 \text{ m s}^{-1}/\text{day}$). The solid contours denote flux divergence, a positive PV flux, and eastward flow acceleration; the dashed contours denote flux convergence and deceleration. (b) The EP flux (arrows) and the time and zonally averaged zonal wind (contours). See the appendix for details of plotting EP fluxes.

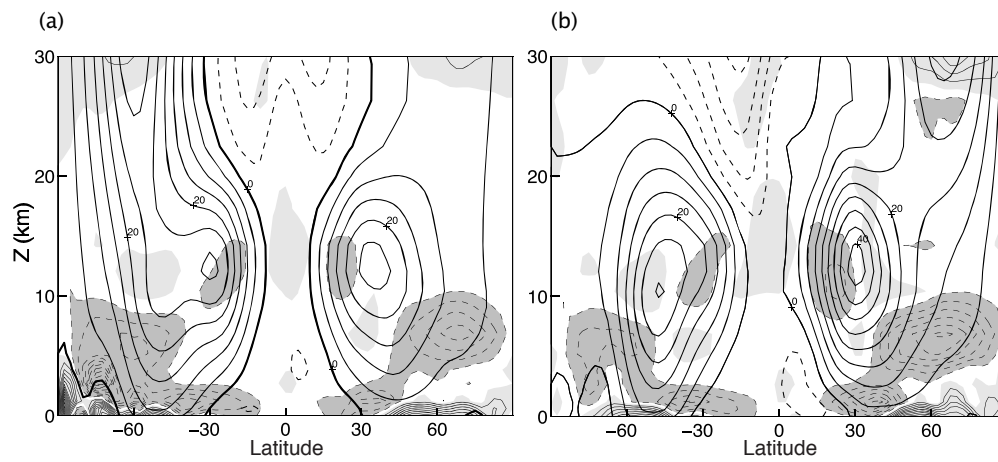


Fig. 12.19 The observed zonally averaged zonal wind (thicker contours, interval 5 m s^{-1}), and the Eliassen-Palm flux divergence (contour interval $2 \text{ m s}^{-1}/\text{day}$, zero contour omitted). Regions of positive EP flux divergence (eastward acceleration) are lightly shaded; regions less than $-2 \text{ m s}^{-1}/\text{day}$ are more darkly shaded. (a) Annual mean, (b) DJF (December-January-February).

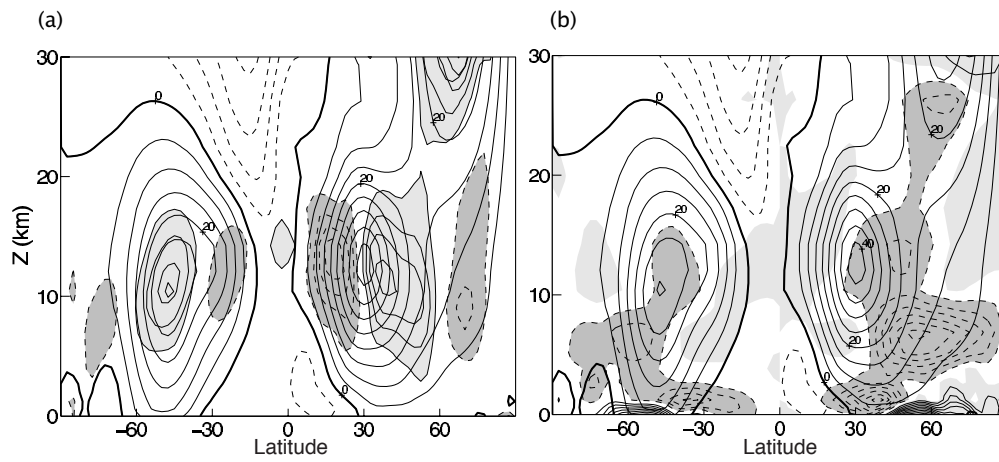


Fig. 12.20 The divergence of the two components of the EP flux (shaded), and the zonally averaged zonal wind (thicker contours) for DJF. (a) The momentum fluxes, $-\partial_y \overline{u'v'}$, contour interval is $1 \text{ m s}^{-1} / \text{day}^{-1}$, light shaded for positive values > 1 , dark shaded for negative values < -1 . (b) The buoyancy flux, $f \partial_z (\overline{v'b'} / N^2)$, with contour interval and shading convention as in Fig. 12.19.

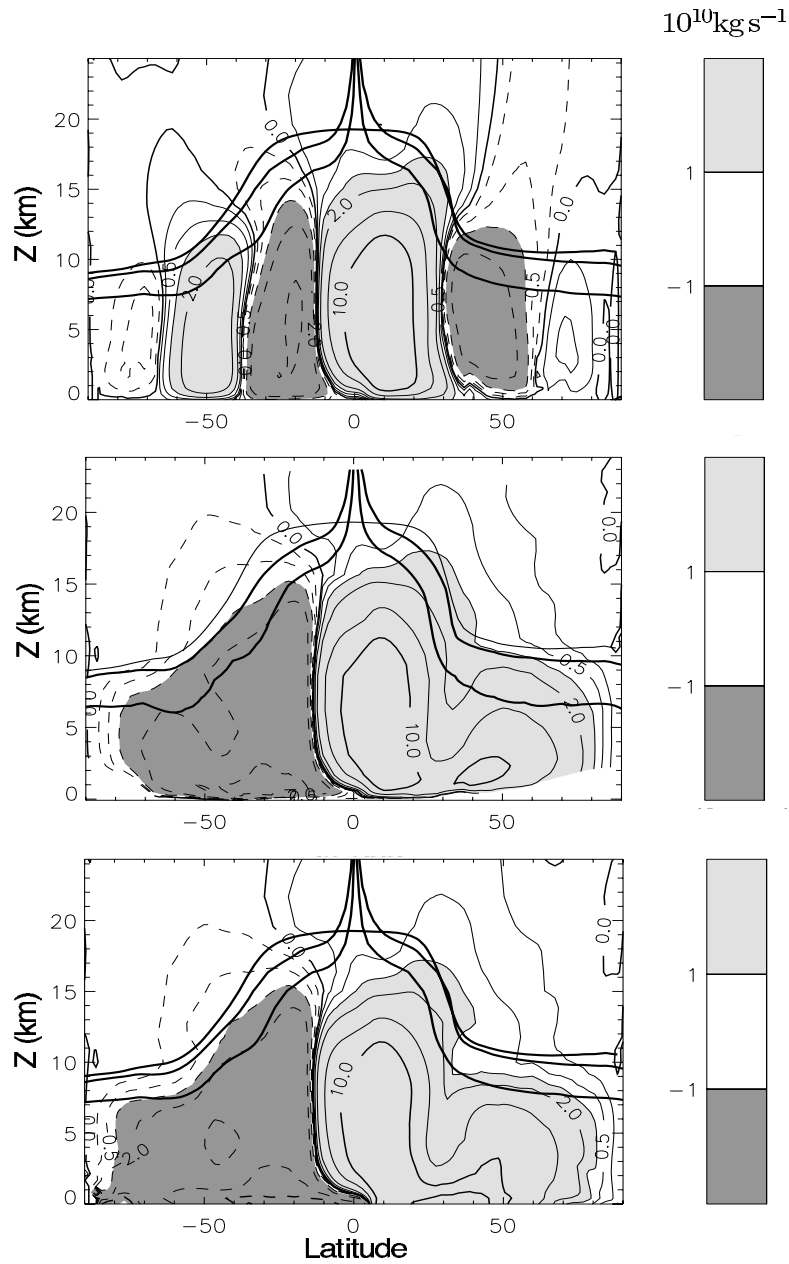


Fig. 12.21 Top: The observed zonally averaged, Eulerian-mean, streamfunction in northern hemisphere winter (DJF, 1994–1997). Negative contours are dashed, and values greater or less than $10^{10} \text{ kg s}^{-1}$ (10 Sv) are shaded, darker for negative values. The circulation is clockwise around the higher shading. The three thick solid lines indicate various measures of the tropopause (section 12.5): the two that peak at the equator are isolines of potential vorticity, $Q = \pm 1.5, \pm 4 \text{ PV units}$, and the flatter one is the WMO thermal tropopause. Middle: The thickness-weighted, or isentropic-mean, meridional mass streamfunction. After calculation in isentropic coordinates, the streamfunction is projected back on to log-pressure coordinates, Z (km), for display. Bottom: the residual streamfunction calculated from the Eulerian circulation and the eddy fluxes.¹

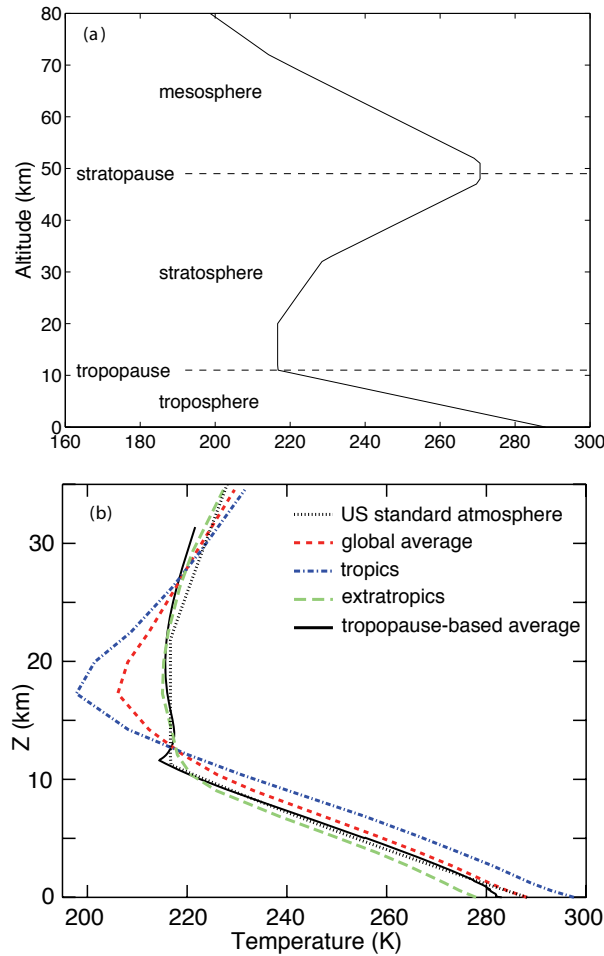


Fig. 12.22 (a) The temperature profile of the ‘U.S. standard atmosphere’, marking the standard regions of the atmosphere below 80 km. In addition to the regions shown, the top of the mesosphere is marked by the mesopause, at about 80 km, above which lies the ‘thermosphere’, in which temperatures rise again into the ‘exosphere’, extending a few thousand kilometres and where the atmospheric temperature ceases to have a useful meaning. (b) Observed, annually averaged profiles of temperature in the atmosphere, where the ordinate is log-pressure. ‘Tropics’ is the average from 30°S to 30°N, and the extratropics is the average over the rest of the globe. The observations are from a reanalysis over 1958–2003 that extends upward to about 35 km. See text for the meaning of ‘tropopause-based average’.

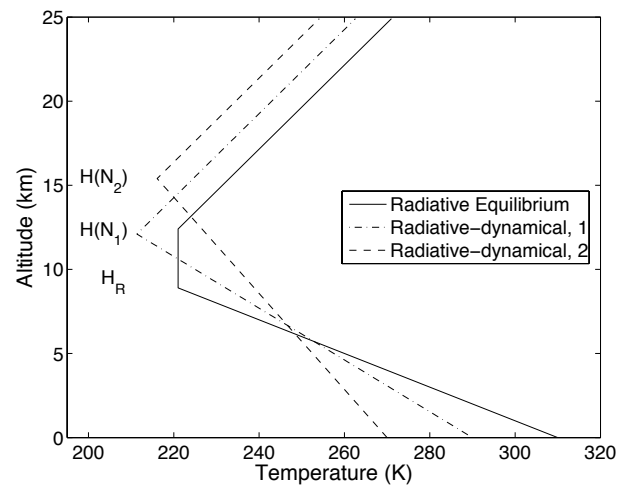


Fig. 12.23 Schema of the radiative equilibrium profile (solid), and two profiles of a radiative-dynamical equilibrium in which the lower atmosphere is adjusted to some specified lapse rate N_1 or N_2 . Here, $N_2 > N_1$ and $H(N_2) > H(N_1)$.

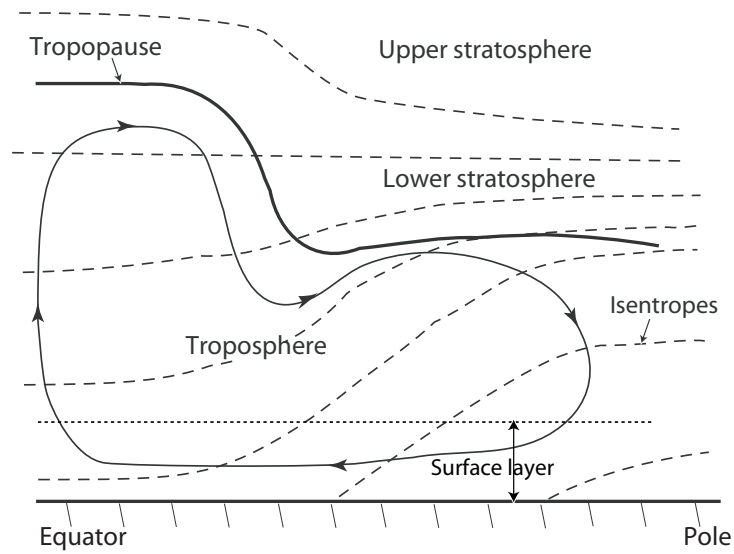


Fig. 12.24 A sketch of the stratification and overturning circulation in the lower atmosphere. The thick line marks the tropopause, the closed contour marks the residual overturning circulation and the dashed lines are isentropes. The overturning circulation has two distinct parts, a tropical Hadley Cell where most of the mass is carried by mean motions, and a shallower extratropical cell in which most of the mass transfer occurs via eddy motion. The equatorwards return flow is mostly confined to a shallow surface layer. The 'lower stratosphere' is ventilated by the troposphere along isentropic surfaces, whereas in the 'upper stratosphere' isentropes do not intersect the tropopause. The tropopause is the boundary between the partially mixed troposphere and the near-radiative equilibrium stratosphere.

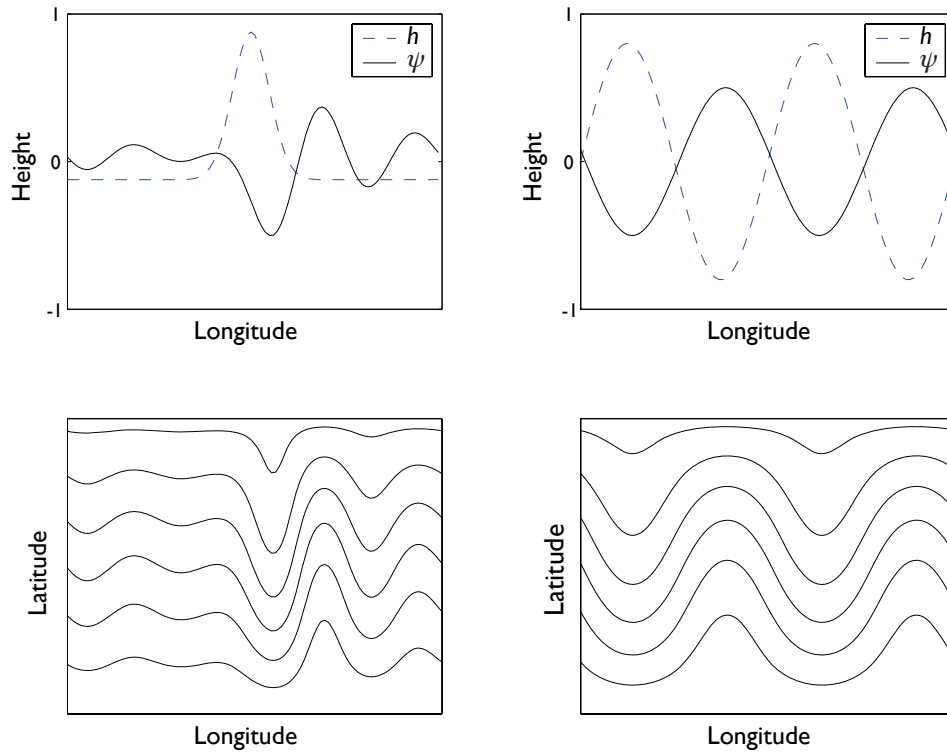


Fig. 13.1 The response to topographic forcing, i.e., the solution to the steady version of (13.10), for topography consisting of an isolated Gaussian ridge (left panels) and a pure sinusoid (right panels). The wavenumber of the stationary wave is about 4 and $r/(\bar{u}k) = 1$. The upper panels show the amplitude of the topography (dashed curve) and the perturbation streamfunction response (solid curve). The lower panels are contour plots of the streamfunction, including the mean flow. With the ridge, the response is dominated by the resonant wave and there is a streamfunction minimum, a 'trough', just downstream of the ridge. In the case on the right, the flow cannot resonate with the topography, which consists only of wavenumber 2, and the response is exactly out of phase with the topography.

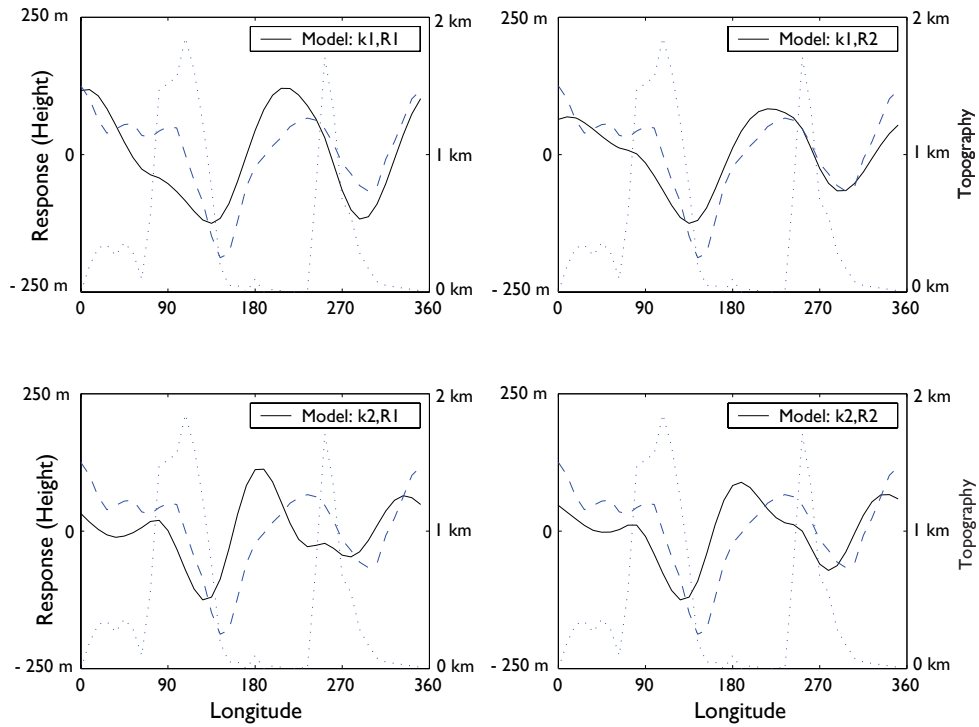


Fig. 13.2 Solutions of the Charney-Eliassen model. The solid lines are the steady solution of (13.10) using the Earth's topography at 45°N with two values of friction ($R1 \approx 6$ days, $R2 \approx 3$ days) and two values of resonant zonal wavenumber (2.5 for $k1$, 3.5 for $k2$), corresponding to zonal winds of approximately 17 and 13 m s^{-1} . The solutions are given in terms of height, η' , where $\eta' = f_0 \psi' / g$, with the scale on the left of each panel. The dashed line in each panel is the observed average height field at 500 mb at 45°N in January. The dotted line is the topography used in the calculations, with the scale on the right of each panel.

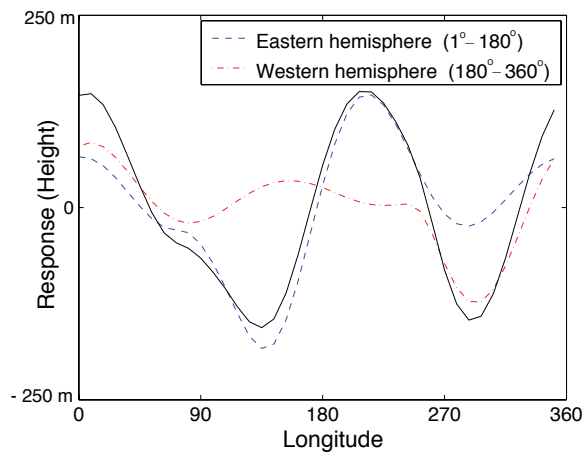


Fig. 13.3 The solution of the upper left-hand panel Fig. 13.2 (solid line), and the solution divided into two contributions (dashed lines), one due to the topography only of the western hemisphere (i.e., with the topography in the east set to zero) and the other due to the topography only of the eastern hemisphere.

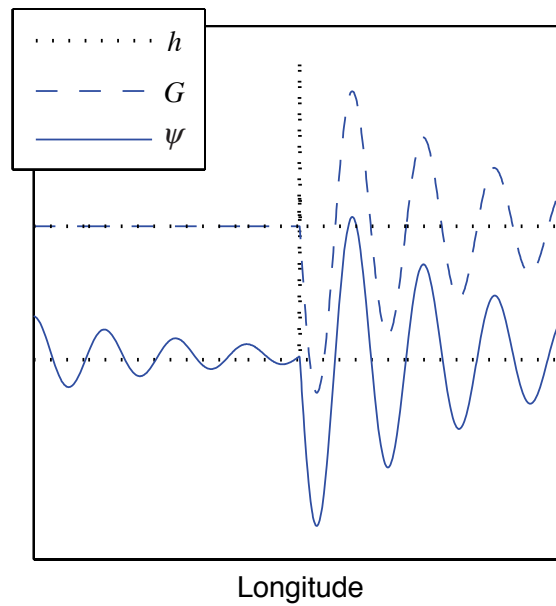


Fig. 13.4 A one-dimensional Rossby wave train excited by uniform eastward flow over a δ -function mountain ridge (h) in the centre of the domain. The upper curve, G , shows the Green's function (13.17), whereas the lower curve shows the exact (linear) response, ψ , in a re-entrant channel calculated numerically using the Fourier method. The two solutions are both centred around zero and offset for clarity; the only noticeable difference is upstream of the ridge, where there is a finite response in the Fourier case because of the progression of the wavetrain around the channel. The stationary wavenumber is 7.5.

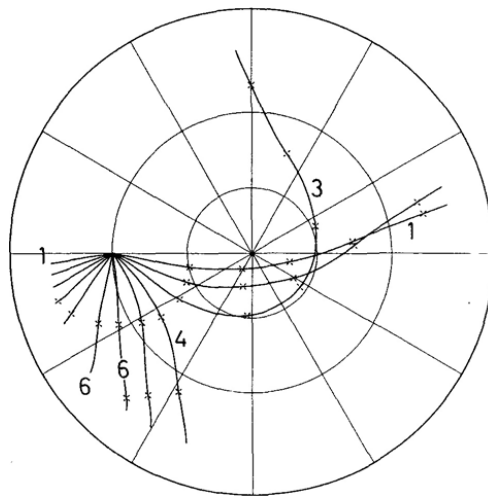


Fig. 13.5 The rays emanating from a point source at 30°N and 180° (nine o'clock), calculated using the observed value of the wind at 300 mb .¹ The crosses mark every 180° of phase, and mark the positions of successive positive and negative extrema. The numbers indicate the zonal wavenumber of the ray. The ray paths may be compared with the full linear calculation shown in Fig. 13.6.

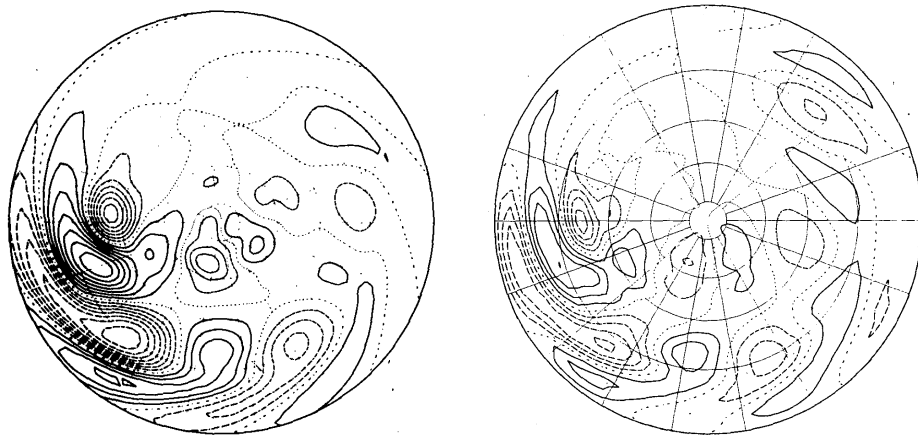


Fig. 13.6 The linear stationary response induced by circular mountain at 30°N and at 180° longitude (nine o'clock). The figure on the left uses a barotropic model, whereas the figure on the right uses a multi-layer baroclinic model.² In both cases the mountain excites a low-wavenumber polar wavetrain and a higher-wavenumber subtropical train.

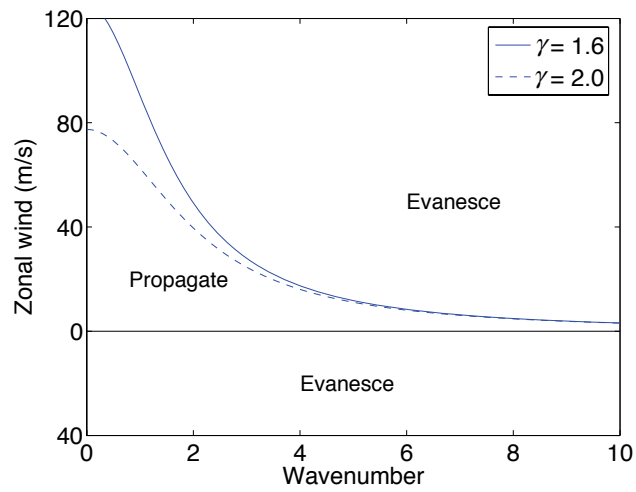


Fig. 13.7 The boundary between propagating waves and evanescent waves as a function of zonal wind and wavenumber, using (13.62), for a couple of values of γ . With $N = 2 \times 10^{-2} \text{ s}^{-1}$, $\gamma = 1.6$ ($\gamma = 2$) corresponds to a scale height of 7.0 km (5.5 km) and a deformation radius NH/f of 1400 km (1100 km).

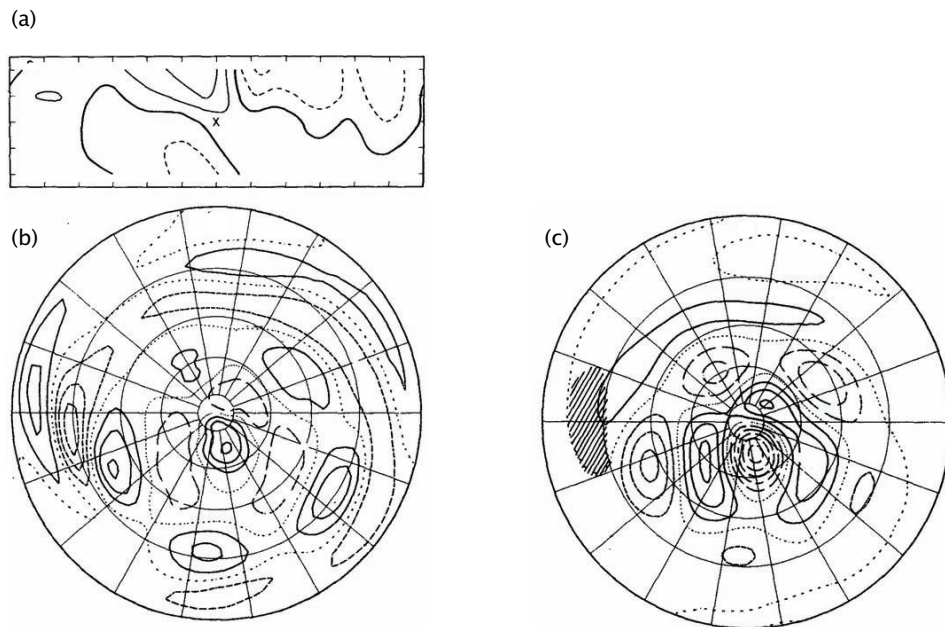


Fig. 13.8 Numerical solution of a baroclinic primitive equation model with a deep heat source at 15°N and a zonal flow similar to that of northern hemisphere winter. (a) Height field in a longitude height at 18°N (vertical tick marks at 100, 300, 500, 700 and 900 mb); (b) 300 mb vorticity field; (c) 300 mb height field. The cross in (a) and the hatched region in (c) indicate the location of the heating.³

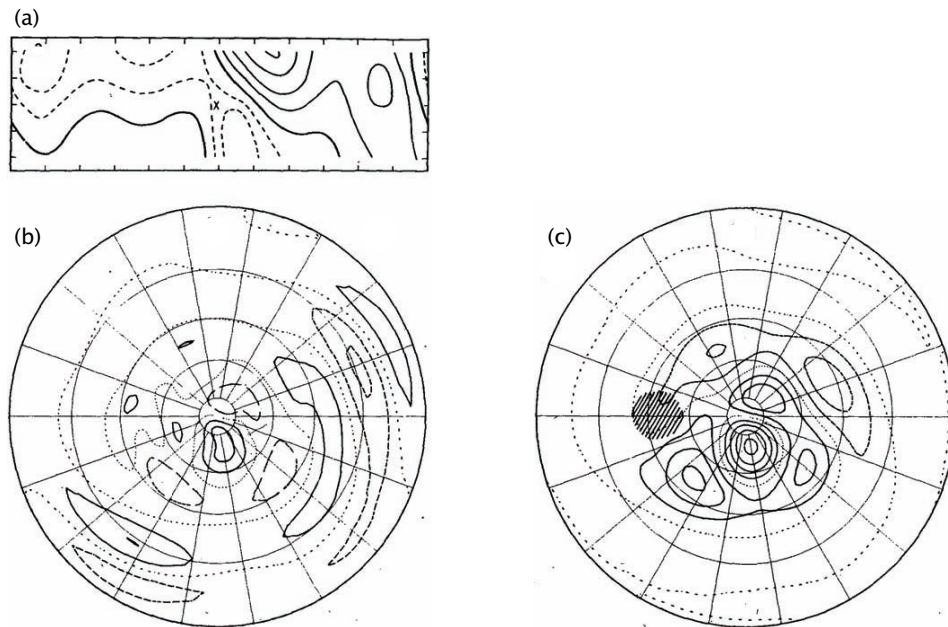


Fig. 13.9 As for Fig. 13.8, but now the solution of a baroclinic primitive equation model with a deep heat source at 45°N. (a) Height field in a longitude height at 18°N; (b) 300 mb vorticity field; (c) 300 mb height field. The cross in (a) and the hatched region in (c) indicate the location of the heating.⁴

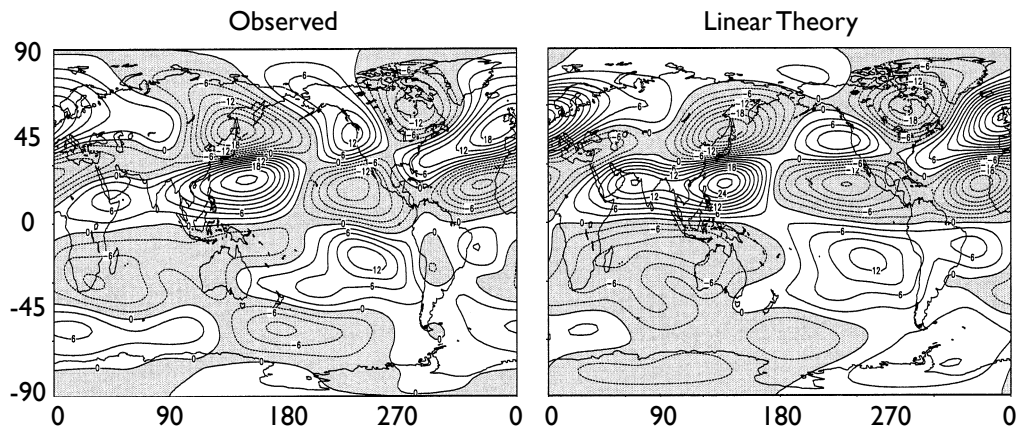


Fig. 13.10 Left: the observed stationary (i.e., time-averaged) streamfunction at 300 mb (about 7 km altitude) in northern hemisphere winter. Right: the steady, linear response to forcing by orography, heat sources and transient eddy flux convergences, calculated using a linear model with the observed height-varying zonally averaged zonal wind. Contour interval is $3 \times 10^6 \text{ m}^2 \text{ s}^{-1}$, and negative values are shaded. Note the generally good agreement, and also the much weaker zonal asymmetries in the southern hemisphere.⁵

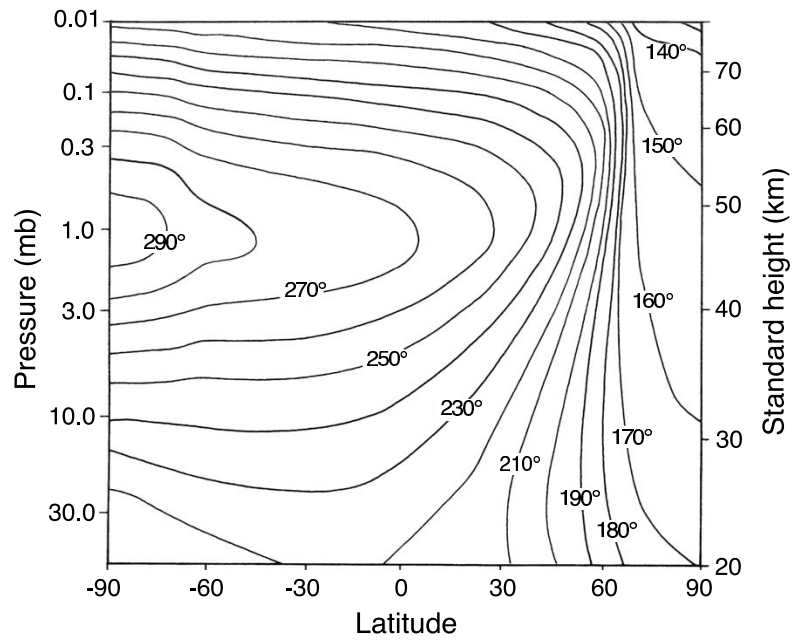


Fig. 13.11 The zonally averaged radiative-equilibrium temperature in in January. The downwards solar radiation at the top of the atmosphere is given, and the upwards radiative flux into the stratosphere is based on observed properties, including temperature, of the troposphere.⁶

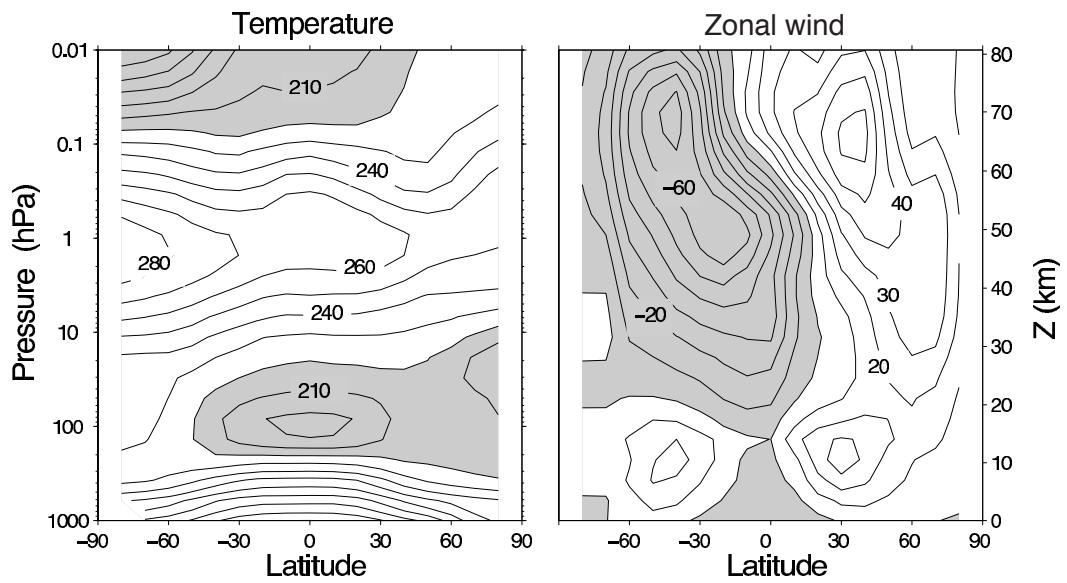


Fig. 13.12 The zonally averaged temperature and zonal wind in January. The temperature contour interval is 10 K, and values less than 220 K are shaded. Zonal wind contours are 10 m s^{-1} and negative (westward) values are shaded.⁷

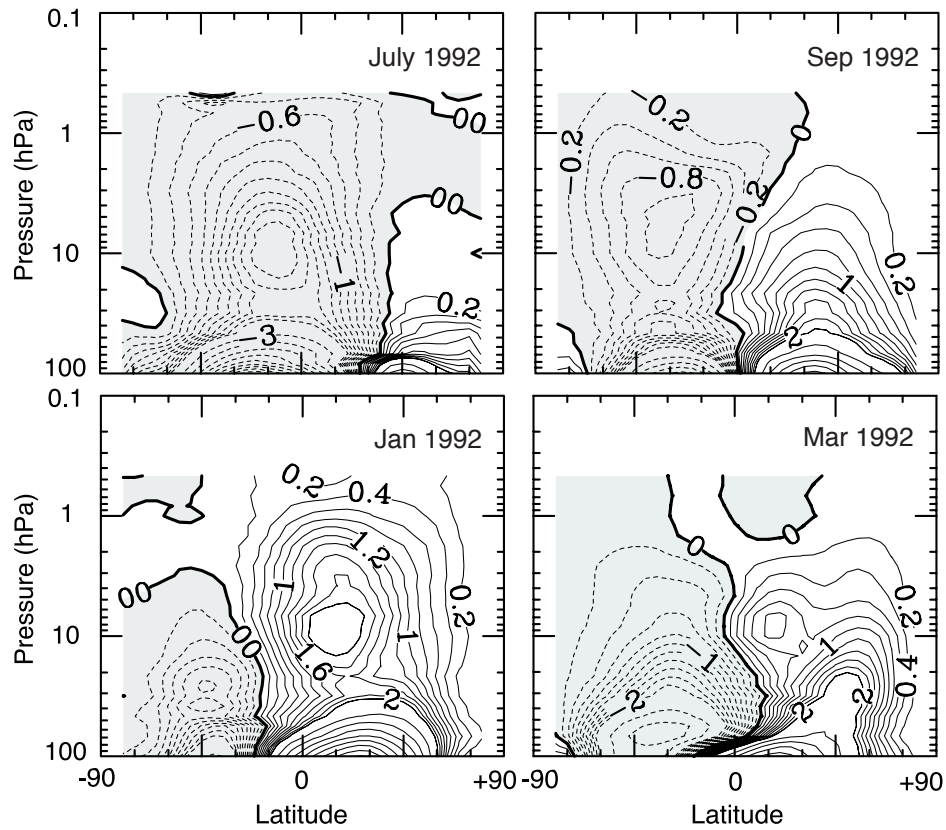


Fig. 13.13 The observed thickness-weighted (residual) streamfunction in the stratosphere, in Sverdrups (10^9 kg s^{-1}). The circulation is clockwise where the contours are solid. Note the stronger circulation in the winter hemispheres, whereas the equinoctal circulations (September, March) are more inter-hemispherically symmetric.⁸

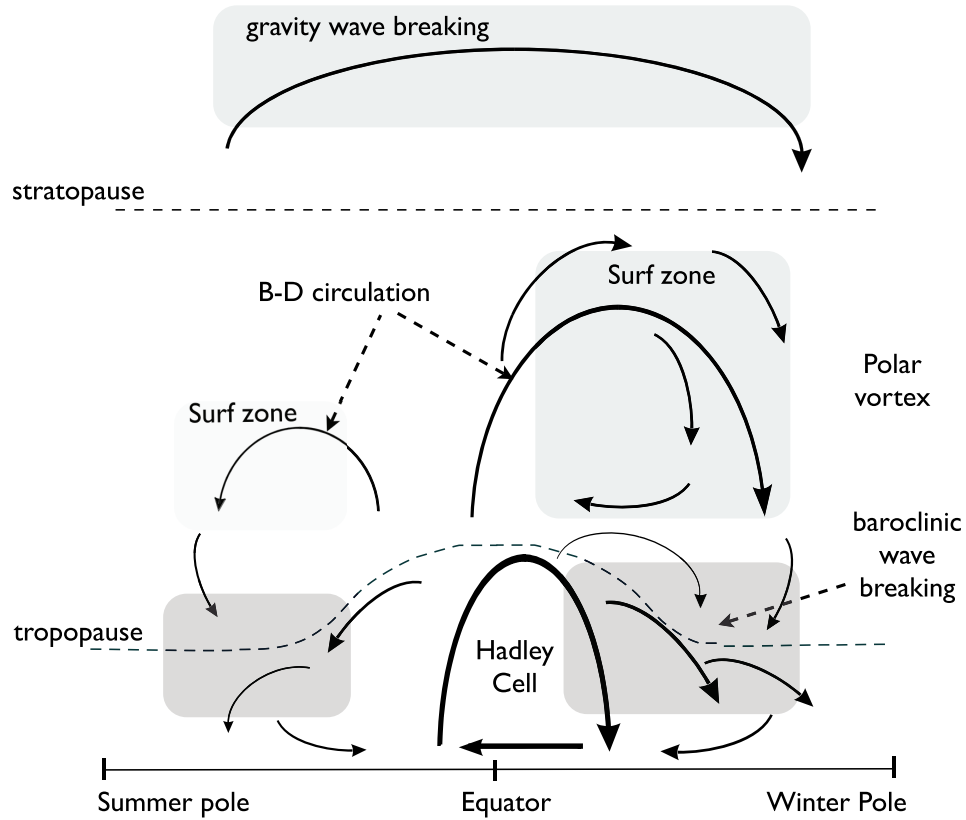


Fig. 13.14 A schema of the residual mean meridional circulation of the atmosphere. The solid arrows indicate the residual circulation (B-D for Brewer-Dobson) and the shaded areas the main regions of wave breaking (i.e., enstrophy dissipation) associated with the circulation. In the surf zone the breaking is mainly that of planetary Rossby waves, and in the troposphere and lower stratosphere the breaking is that of baroclinic eddies. The surf zone and residual flow are much weaker in the summer hemisphere. Only in the Hadley Cell is the residual circulation comprised mainly of the Eulerian mean; elsewhere the eddy component dominates.⁹

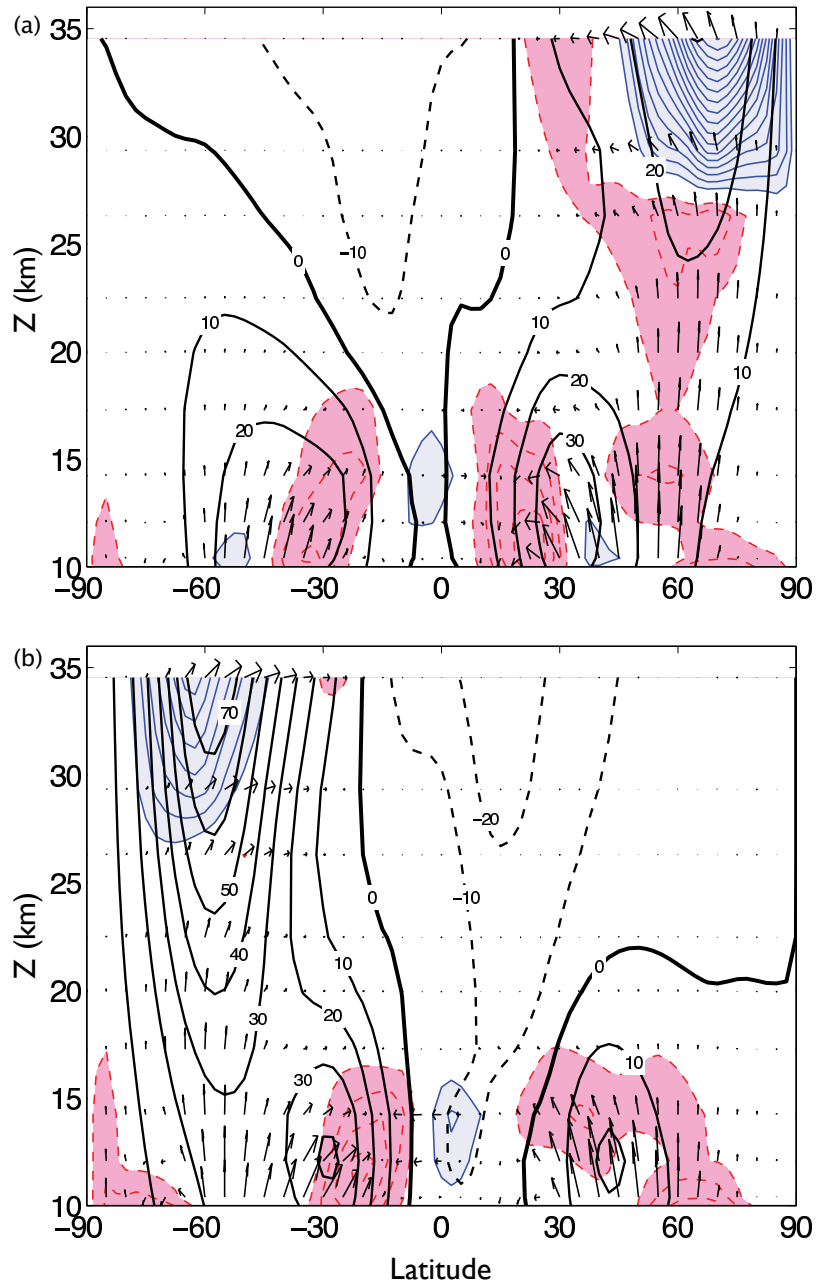


Fig. 13.15 The EP flux vectors (arrows), the EP flux divergence (shaded and light contours) and the zonally averaged zonal wind (heavy contours) for (a) northern hemisphere winter; (b) southern hemisphere winter. Note the almost zero EP values in the summer hemispheres, and strong convergence at high latitudes in the winter hemispheres, leading to polewards residual flow and/or zonal flow acceleration. The EP divergence is shaded for values greater than $+1 \text{ m s}^{-1}/\text{day}$, light solid contours) and for values less than $-1 \text{ m s}^{-1}/\text{day}$ (light dashed contours). The vertical coordinate is log pressure, extending between about 260 and 10 mb.

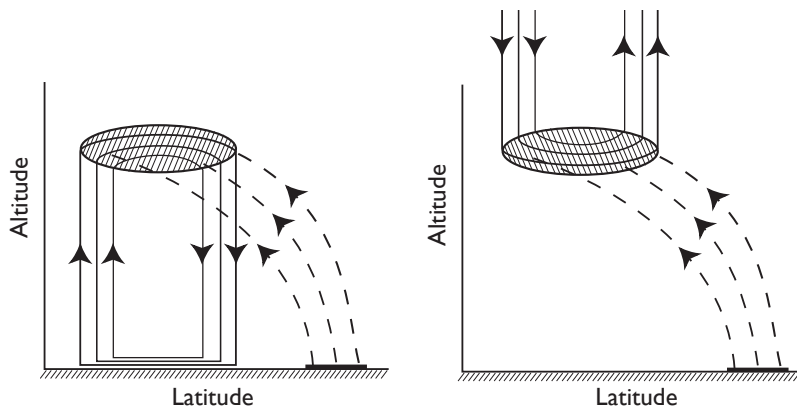


Fig. 13.16 Idealized example of downward control. Left panel: wave activity propagates upward (dashed lines) from a tropospheric source, breaking and depositing zonal momentum in the shaded region. This induces an overturning circulation (solid lines) below the region of momentum deposition, connecting the region of wave breaking with a frictional boundary layer. Right panel: putative 'upward control', which would require a frictional sink above the wave breaking region.

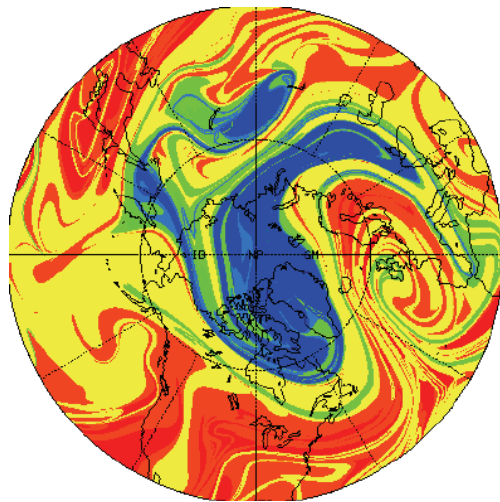


Fig. 13.17 The tracer distribution in the northern hemisphere lower stratosphere on 28 January 1992. The tracer was initialized on 16 January by setting it equal to the potential vorticity field calculated from an observational analysis, and then advected for 12 days by the observed wind fields.¹⁰

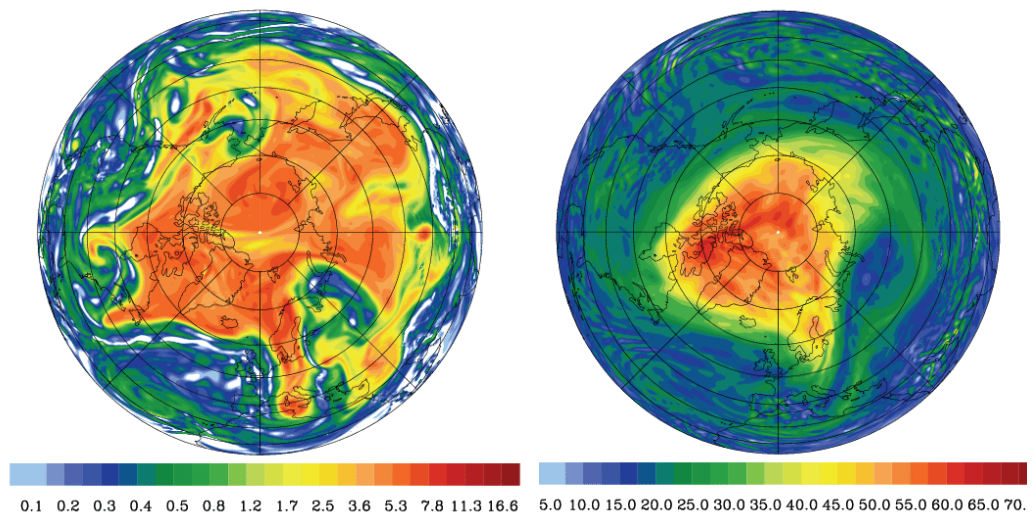


Fig. 13.18 The potential vorticity on two isentropic surfaces, the 310K surface (left) and the 475K surface (right), on January 19, 2005. The shaded bar is in PV units. The 310K surface is mainly in the troposphere (see Fig. 12.16) where baroclinic instability is abundant. The 475K surface is at about 20 km altitude, and on it we see a polar stratospheric vortex with a fairly sharp boundary where the PV gradient is high, and a mid-latitude region of smaller-scale features and wave breaking.¹¹

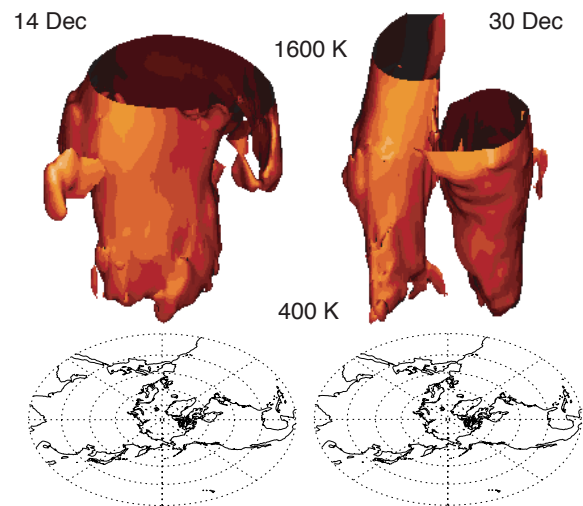


Fig. 13.19 The edge of the stratospheric polar vortex in 1984. Plotted is the 35 PVU isosurface of $Q^* = Q(\theta/\theta_0)^{4.1}$, where Q is Ertel PV and $\theta_0 = 475$ K. The vertical coordinate is potential temperature. Like Q , Q^* is materially conserved in adiabatic flow. It is approximately constant at the vortex edge, roughly compensating for the change in density with height that affects the Ertel PV. The left panel shows the vortex in a fairly usual state, and the right panel shows a split vortex following a stratospheric sudden warming.¹²